Journal of Materials Chemistry A

Surface engineering of MXenes for energy and environmental applications

Journal:	*Journal of Materials Chemistry A*
Manuscript ID	TA-REV-02-2022-001140.R1
Article Type:	Review Article
Date Submitted by the Author:	31-Mar-2022
Complete List of Authors:	Su, Tongming; Guangxi University, Ma, Xiaohan; Oak Ridge National Laboratory Tong, Jianhua; Clemson University, Materials Science and Engineering; Clemson University, Materials Science and Engineering Ji, Hongbing; Sun Yat-sen University, School of Chemistry Qin, Zu-Zeng; Guangxi Univeristy, School of Chemistry and Chemical Engineering Wu, Zili; Oak Ridge National Laboratory, Chemical Science Division and Center for Nanophase Materials Sciences

Surface engineering of MXenes for energy and environmental applications

Tongming Su[1†], Xiaohan Ma[2, 3†], Joshua Tong[3]*, Hongbing Ji[1, 4], Zuzeng Qin[1]*, Zili Wu[2]*

1. School of Chemistry and Chemical Engineering, Guangxi Key Laboratory of Petrochemical Resource Processing and Process Intensification Technology, Guangxi University, Nanning 530004, P. R. China

2. Center for Nanophase Materials Sciences, Oak Ridge National Laboratory, Oak Ridge, Tennessee 37831, USA

3. Department of Materials Science and Engineering, Clemson University, Clemson, South Carolina 29634, USA

4. Fine Chemical Industry Research Institute, School of Chemistry, Sun Yat-sen University, Guangzhou 510275, P. R. China

[†]equal contribution

*Corresponding author:

E-mail: wuz1@ornl.gov (Z. Wu), jianhut@clemson.edu (J. Tong), qinzuzeng@gxu.edu.cn (Z. Qin)

ABSTRACT: MXenes, a new family of two-dimensional (2D) transition-metal carbides, nitrides, and carbonitrides, have received considerable attention in the energy and environmental applications due to their intriguing electronic, electrochemical, optical, and chemical properties. Applications of MXenes have been witnessed in photocatalysis, electrocatalysis, thermocatalysis, sensing and biosensing, electrochemical energy storage, energy conversion and storage, rechargeable batteries, supercapacitors, and biomedicine. Notably, the tunable surface chemistry of MXenes plays an important role in their success in those applications. The surface composition of MXenes is considered to have a significant influence on their physicochemical properties and functionalities. In order to achieve a comprehensive understanding and the rational design of MXenes by surface engineering, in this review, we highlight the application of several kinds of surface engineering approaches for MXenes, including tuning the surface termination groups, surface functionalization, surface defects, surface doping, surface oxidation, and the theoretical simulation of surface engineering of MXenes. Moreover, the relationship between the surface engineering and the physicochemical properties of the MXenes is discussed. Finally, the ongoing challenges and opportunities for the future development of MXene surface engineering are also proposed.

KEYWORDS: surface engineering; MXenes; energy; environmental; two-dimensional

1. Introduction

Two-dimensional (2D) materials have attracted significant attention due to their attractive properties. Inspired by the discovery of freestanding single-layer graphene, many other 2D materials were found, such as 2D transition metal dichalcogenides[1], layered double hydroxides[2], hexagonal boron nitride[3], transition metal oxides[4], nitrides[5], and MXenes[6]. Since the discovery of MXenes (transition metal carbides, nitrides, and carbonitrides) in 2011[7], MXenes have attracted great attention due to their intriguing electronic and structural properties, such as high electrical conductivity, hydrophilic nature, large surface area, and easily tunable structure. During the past years, MXenes have been studied by many researchers in various fields, such as batteries, supercapacitors, electromagnetic interference shielding, photothermal conversion, electrocatalysis, and photocatalysis. Therefore, a fast development has been witnessed with these emerging and promising 2D materials – MXenes[8-12].

MXenes ($M_{n+1}X_n$, n=1~3) were originated from the MAX phases (M, transition metal; A, A-group element; X, C or N), where the $M_{n+1}X_n$ are interleaved with the A layers. Therefore, MXenes can be synthesized by removal of the A-layers from the MAX phases through a chemical etching[13, 14]. A variety of etching agents have been used for the etching of MAX phases, such as HF[15], LiF/HCl[16, 17], and NH_4HF_2[18, 19]. After etching, the surface of MXenes was terminated with O^{2-}, OH^-, F^-, or NH_4^+, and it is possible that these functional groups are intercalated between the MXene sheets. In general, the obtained MXene sheets are designated $M_{n+1}X_nT_x$, where T_x refers to the surface groups. To date, a variety of MXenes have been fabricated, such as Ti_3C_2, Ti_2C, and Nb_2C among others. The preparation methods of various MXenes were summarized in previous reviews[13, 14, 19-22].

The physicochemical properties of MXenes depend greatly on the chemical nature of their surface. For example, the work function of MXenes can be adjusted by tailoring surface terminations. The work

function of OH-terminated $Ti_{n+1}C_n$ MXene is between 1.6 and 2.8 eV, which is much lower than that of O-terminated $Ti_{n+1}C_n$ MXene (5.75 ~ 6.25 eV)[23]. Many reviews on MXene-based materials have been published with different foci such as the synthesis of MXenes[13, 19, 24, 25], the applications of MXenes in photocatalysts[26, 27], sensing and biosensing[28], electrochemical microsupercapacitors[29], energy conversion and storage[30-34], thermocatalysis[35], sensor and chemical adsorption[36], rechargeable batteries and supercapacitors[37], biomedical applications[38], and environmental applications[39]. However, to our knowledge, no review has been focused on the surface engineering aspect of MXenes for the above-mentioned applications.

This review provides a systematic summary of the surface engineering of MXenes, including the surface termination groups, surface functionalization, surface defects, surface doping, surface oxidation, and the theoretical calculation of MXene surface engineering. The consequences of these surface engineering of MXenes are discussed on the physiochemical properties and performances in the energy and environmental applications. Moreover, the ongoing challenges and opportunities for the future development of MXene surface engineering are also proposed. Notably, a recent topical review on the surface and heterointerface engineering of 2D MXenes was reported[40]. However, this review focuses mainly on the application of MXene-based nanocomposites on the electro- and photocatalysis, and only the surface termination groups were mentioned, i.e., other approaches for surface engineering of MXenes were not summarized. Therefore, we believe that a comprehensive review to survey the surface engineering of MXenes systematically is timely to promote further developments of this exciting and still emerging area of research.

2. Surface termination groups of MXenes

It is well known that MXenes prepared by traditional etching with HF or HCl/LiF as etchant will

leave surface terminations, namely -O, -OH, and -F, that bonded to the surface metal atoms of MXenes, as illustrated in Fig. 1[41-44]. Based on theoretical simulation and experiment results, some reports showed that these terminations are "harmful" to the electric properties of MXenes such as electrical conductivity[45-47], electron mobility[48], and Li-ion conductivity[49], which impedes the application of this material as an electrode. Therefore, extensive works have been done to partially remove the terminations on the MXene surface in order to improve the electric performance. For example, Lu et al.[50] and Kong et al.[51] successfully increased the specific capacity of the lithium-ion battery (up to 69%) by decreasing the -F and -OH content on the $Ti_3C_2T_x$ anode. Hart et al.[52] and Halim et al.[53] experimentally proved that the electrical conductivity of MXenes increased in accordance with the decrease of the surface termination. Therefore, by partially removing the surface terminations, the electrical conductivity of MXenes can be improved.

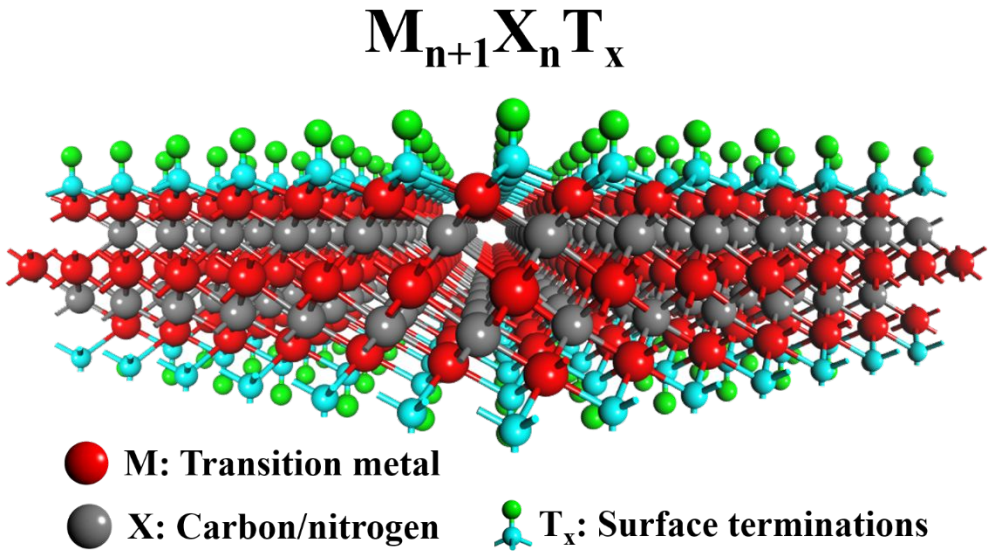

Fig. 1 Schematic illustration of the $M_{n+1}X_nT_x$ MXene structures, where M is an early transition metal, X is carbon and/or nitrogen, and T_x represents surface terminations of the outer metal layers.

Furthermore, the abundant terminations can also impart more features to MXenes. -O termination

has been theoretically proved to be beneficial for the Li-ion storage of $Ti_3C_2T_x$ and M_2CT_x (M = Sc, Ti, V and Cr)[54, 55]. Wang et al. experimentally proved that $Ti_3C_2T_x$ with O-rich surface demonstrated higher Li-ion storage than its F-rich and OH-rich counterparts[56]. Meanwhile, -OH termination can enhance the performance of $Ti_3C_2T_x$ in chemisorption through ion exchange process[57-64]. Usually, -OH, along with -O, are referred as oxygen-containing terminations since their chemical and electrochemical behaviors are similar on the surface of MXenes. Both of them can make $Ti_3C_2T_x$ a promising material as electrochemical capacitor[65-67] and sensor[68]. Recently, even the long-time ignored -F termination has been experimentally proved by Li et al.[69] to be contributive to the electrocatalytic hydrogen evolution reaction (HER) performance of Ti_2CT_x.

In addition, it was demonstrated by DFT calculation that the Fermi levels (E_F) of MXene and the Gibbs free energy of the intermediate state H*, |ΔGH*| depended on the surface termination (such as -O and -F) of MXene[70, 71]. For example, the E_F of Ti_3C_2 was calculated to be -0.05 V versus standard hydrogen electrode (SHE), while the E_F of the O- and F-terminated Ti_3C_2 was calculated to be 1.88 and 0.15 V versus SHE[70], respectively. The more positive value of E_F indicated stronger ability of MXenes to accept photogenerated electrons from the semiconductor photocatalysts. Therefore, the O-terminated Ti_3C_2 was a better cocatalyst for the photocatalyst to capture the photogenerated electrons compared to pure Ti_3C_2 and F-terminated Ti_3C_2. Meanwhile, the ΔGH*, which was considered as the major indicator for the hydrogen production activity, was changed from -0.927 eV for pure Ti_3C_2 to 1.995 eV and 0.003 eV for the F-terminated Ti_3C_2 and O-terminated Ti_3C_2, respectively. The value of 0.003 eV is close to zero, indicating the potentially remarkable HER activity of O-terminated Ti_3C_2 from the viewpoint of thermodynamics.

Therefore, these surface terminations are essential to the properties of MXenes, and deliberate

manipulation of the surface terminations can make it a versatile material. In this section, we summarize some popular methods that have been confirmed effective for termination regulation.

2.1 Regulation of surface termination by alkalization

Alkalization is the most popular and facile post-treatment method to increase the -OH population on MXene surface. This treatment can not only enhance the chemical and/or electrochemical performance of MXenes, but also protect the bare surface Ti atoms from oxidation in air[62]. It has even been reported that this treatment is capable of altering the morphology of MXenes, creating more contacting points when introduced to the surface of another material to form a composite[72]. This method targets at the MXene that originally has -F terminations and consists of two simultaneous processes: surface termination substitution and ion intercalation. Since -F is not stable under high pH value, it will be eventually replaced by -OH[55, 61] under alkaline condition. Although intercalation is seemingly irrelevant to the surface group manipulation, it is always coupled with alkalization as the metal ions in alkaline like LiOH[57, 73], NaOH[57, 62, 64, 68, 69, 72, 74-77], and KOH[57, 58, 65, 78-80] will spontaneously move into the interlayer space, partially replacing H in -OH through ion exchange, hence simultaneously expanding interlayer distance. Apart from alkaline, Dall'Agnese et al.[65] proved that salt like KOAc (Ac= acetate), which can produce -OH during hydroxylation, had a similar effect on MXenes as well. Therefore, by immersing MXenes in an alkaline solution with a certain concentration and stirring for a certain duration of time under a desired temperature, MXenes with -OH rich surface and expended interlayer space can be achieved.

O/F ratio on the surface of MXenes detected by either X-ray Photoelectron Spectroscopy (XPS) or Energy-Dispersive X-ray Spectroscopy (EDX) after the alkalization can be used as a criterion when evaluating the F-OH substitution degree of this process. However, compared with EDX, XPS can

provide more comprehensive information of the surface chemistry. Thus, unless specifically marked as "EDX", the O/F ratios in Table 1 are obtained by XPS. It straightforwardly manifests the ratio of the sum of -OH and -O to -F. Since -O is immune to the alkalization, it is reasonable to state that the higher the resulting O/F ratio is, the larger portion of -OH has been introduced to the surface of MXenes, implying a more complete alkalization process. Table 1 summarizes several sets of alkalization parameters and the resulting O/F ratios. Clearly, different groups of parameters result in highly dispersive O/F ratios. Therefore, it is of great value to figure out how these parameters affect the extent of alkalization so that one may deliberately design a process that can maximize the F-OH substitution. Since the interlayer expansion will increase the contact area of MXenes with the alkaline solution, there is a good reason to believe that the intercalation will further facilitate the alkalization. However, even though the ion sizes of Li^+, Na^+, and K^+ obviously differ from each other and offer potentially different lattice expansions, results from Wei et al.[57] suggest that little impact is brought by them to the O/F ratio after the alkalization (Entry 3, 12 & 16 in Table 1). They made a direct comparison of $Ti_3C_2T_x$ treated with different alkalis in order to optimize its adsorption capacity of methylene blue. Although all of them successfully increased the O/F ratio of the untreated $Ti_3C_2T_X$, the difference between them did not follow the same fashion with the change of lattice expansion (depicted by c-lattice constant increase) and was almost negligible. The highest interlayer expansion percentage (regarding the untreated MXenes) was achieved by LiOH due to the smallest cation size of Li^+, whereas NaOH achieved the highest O/F ratio. The highest O/F ratio of NaOH-treated $Ti_3C_2T_x$ led to its highest adsorption capacity (ca. 189 mg/g vs. 100 mg/g for the untreated one). Therefore, the larger interlayer spacing cannot guarantee higher F-OH substitution completeness. This fact may suggest that even for the lowest interlayer distance achieved by K^+, there was enough space for the process.

Table 1. Summary of the MXene alkalization conditions and the respective O/F ratios.

Entry	Alkaline	MXene	Reaction conditions§	O/F ratio change		Ref.
				Original	Alkalized	
1	NaOH	Ti_2CT_X	1 M, RT*, 2 h	0.14 (EDX)	6.30 (EDX)	69
2	NaOH	$Ti_3C_2T_X$	5 M, RT, 2 h	2.60	7.69	68
3	NaOH	$Ti_3C_2T_X$	1 M, 80 °C, 1 h	0.34	1.02	57
4	NaOH	$Ti_3C_2T_X$	1 M, 60 °C, 4 h	6.64	14.92	74
5	NaOH	$Ti_3C_2T_X$	1.25 M, RT, 2 h	0.68	5.75	64
6	NaOH	$Ti_3C_2T_X$	1.25 M, 20 °C, 4 h	2.57 (EDX)	4.77 (EDX)	77
7	NaOH	$Ti_3C_2T_X$	1 M, RT, 10 min	1.41 (EDX)	5.35 (EDX)	72
8	NaOH	$Ti_3C_2T_X$	3 M, RT, 10 min	1.41 (EDX)	8.87 (EDX)	72
9	NaOH	$Ti_3C_2T_X$	5 M, RT, 10 min	1.41 (EDX)	18.66 (EDX)	72
10	NaOH	$Ti_3C_2T_X$	7 M, RT, 10 min	1.41 (EDX)	13.55 (EDX)	72
11	KOH	$Ti_3C_2T_X$	2M, RT, 12 h	0.98	8.03	80
12	KOH	$Ti_3C_2T_X$	1 M, 80 °C, 1 h	0.34	0.92	57
13	KOH	$Ti_3C_2T_X$	0.9 M, RT, 24 h	1.22	8.88	58
14	KOH	$Ti_3C_2T_X$	6 M, RT, 72 h	N/A	6.32 (EDX)	78
15	KOH	V_2CT_X	1 M, RT, 24 h	0.52	9.51	79
16	LiOH	$Ti_3C_2T_X$	1 M, 80 °C, 1 h	0.34	0.94	57

*: RT - room temperature;

§: Reaction conditions are given as alkali concentration, reaction temperature and reaction time

The seemingly more influential factor for O/F ratio is alkali concentration. Li et al.[69] conducted the alkalization with 1M NaOH for 2 h under room temperature to achieve an O/F ratio around 6.30. By slightly increasing the concentration of NaOH to 5 M (the other parameters kept the same), a higher O/F ratio of 7.69 was achieved by Yang et al.[68], enhancing the humidity sensitivity of $Ti_3C_2T_x$ by up to 60 times. Xiang et al[72] (entry 10 in Table 1) investigated in more details the impact brought by NaOH concentration. The original O/F ratio of the $Ti_3C_2T_x$ was 1.41. After 10 min alkalization under RT with 1, 3, and 5 M NaOH, the O/F ratio was elevated to 5.35, 8.87 and 18.66, respectively. However, as they further increased the concentration to 7 M, the resulting O/F ratio decreased to 13.55. As a consequence, the highest O/F ratio produced the most wrinkles on $Ti_3C_2T_x$, making it a better candidate than all the counterparts for piezoresistive sensor fabrication. This result suggested that the completeness of alkalization is partially dependent on the alkali concentration. However, there may be an inflection point, beyond which the dependence will not be obvious anymore. This trend may also be consolidated by comparing entry 1 & 2 in Table 1.

Currently, the partial contribution from reaction temperature and time of alkalization remains unknown due to the lack of available research data. Comparing entry 1, 7 and 15 in Table 1, longer reaction time is seemingly helpful to increase the O/F ratio. Meanwhile, if comparing entry 2 and 9, longer reaction time leads to lower O/F ratio. This disagreement may be caused by other factors imbedded in how the material was prepared and how the alkalization was actually conducted, which is far more complicated. Thus, Table 1 is only a summary of some selected parameters and no solid trend of time and temperature factors can be concluded unless a direct comparison is made as in ref [57] and ref [72].

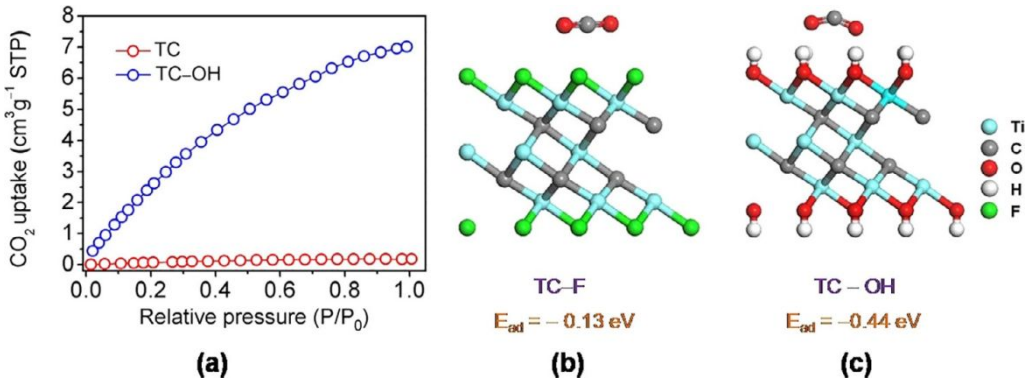

Fig. 2 a) CO_2 adsorption behaviors for TC and TC-OH. b,c) Side view of the adsorption models of CO_2 on 2×2×1 TC@F (b) and 2×2×1 TC@OH supercells (c). Reproduced with permission from ref.[81], Copyright © 2018 Wiley-VCH Verlag GmbH & Co. KGaA, Weinheim.

Surface-alkalinized Ti_3C_2 MXene was proved to be an efficient cocatalyst of P25 for photocatalytic CO_2 reduction by Ye et al[81]. In their work, the -F on the surface of the Ti_3C_2 (TC) was replaced by -OH to obtain the Ti_3C_2-OH (TC-OH) when the Ti_3C_2 was treated with KOH. When the TC surface was terminated with -OH, the adsorbing capacity of CO_2 was greatly enhanced from 0.18 cm^3g^{-1} (TC) to 7.01 cm^3g^{-1} (TC-OH), as shown in Fig. 2. Moreover, according to the DFT calculations, the adsorption energy of CO_2 (-0.13 eV) on TC-F was smaller than that of CO_2 on TC-OH (-0.44 eV) (Fig. 2). Therefore, the higher adsorption capability of CO_2 on TC-OH might be ascribed to the stronger adsorption of CO_2 on TC-OH. In addition, based on the FTIR results, more carbonate species, characterized by vibrational modes of $\nu_s(CO_3)$ (ca. 1320 cm^{-1}) and $\nu_{as}(CO_3)$ (ca. 1580 cm^{-1}), can be generated on the 5TC-OH/P25 than that of 5TC/P25 after irradiation, indicating that CO_2 is easily converted to the activated CO_3^{2-} on 5TC-OH/P25 sample. With the 5TC-OH/P25 as the photocatalyst for CO_2 reduction reaction, the evolution rates of CO (11.74 μmol g^{-1} h^{-1}) and CH_4 (16.61 μmol g^{-1} h^{-1}) were 3 and 277 times higher than those of bare P25, respectively.

Due to its high work function, MXene have been widely used as the electron receiver cocatalyst

of semiconductor photocatalysts[82]. However, the work function of the MXene can also be altered by alkalization. When the surface termination of the MXene was replaced by -OH, the work function of the MXene was greatly decrease. For example, based on the results of ultraviolet photoelectron spectroscopy (UPS), the work functions of the $Ti_3C_2M_x$ (M = O, -F, –OH) and $Ti_3C_2T_x$ (T = -OH) was calculated to be 3.51 and 2.28 eV, respectively[83]. In this case, when the $Ti_3C_2T_x$ was used as the cocatalyst for the TiO_2 (work function = 4.27) , the $Ti_3C_2T_x$ was acted as the hole trapping instead of electron receiver.

2.2 Regulation of surface termination by thermal treatment

Thermal treatment or annealing is a feasible strategy to remove the surface termination partially. By deliberately designing an annealing temperature program, the composition of surface terminations can be manipulated because the stability of these terminations is different from each other. Density functional theory (DFT) calculation results from Hu et al.[84] showed that among $Ti_3C_2(OH)_2$, $Ti_3C_2F_2$, and $Ti_3C_2O_2$, $Ti_3C_2(OH)_2$ is the most unstable one, whereas the $Ti_3C_2O_2$ is the most stable one. Similarly, Ashton et al.[85] claimed that for Ti_2CT_x MXene, these terminations followed the same fashion as mentioned above based on their DFT calculations. Additionally, they even proposed that for all MXenes (except M = Sc), -O is preferred over other terminations. Some experimental results also consolidated that during heat treatment under an inert atmosphere or vacuum, -OH will be converted to -O[50], which can resist relatively higher temperatures[52, 86]. It should be noticed that MXenes are vulnerable to oxidation when annealed under air; hence only annealing processes under an inert atmosphere are discussed in this section.

Currently, the temperatures of dissociation onset of the three typical terminations over MXenes are not well-defined. Therefore, only a possible range of the onsets will be provided in this section.

Generally, based on the information from Thermogravimetric Analysis (TGA), Thermogravimetric Analysis-Mass Spectrometry (TGA-MS), Differential Scanning Calorimetry (DSC), and Thermogravimetric Analysis-Differential Scanning Calorimetry (TGA-DSC), the onset of different surface species can be determined.

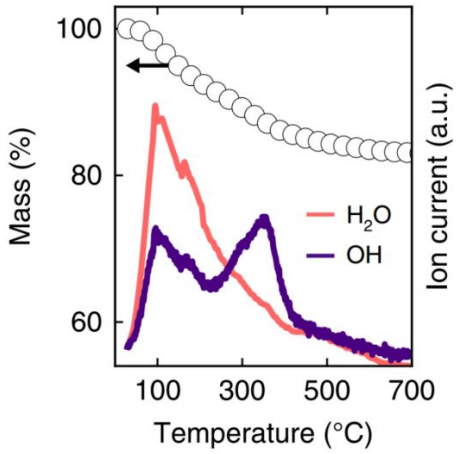

Fig. 3 Influence of heat treatment on -OH terminations (a) TGA-MS of Ti_3CNT_X under He. Reproduced with permission from ref. [52], Copyright © 2019, The Author(s).

The dissociation of -OH is approximately around 200 – 400 °C for Ti MXene species[51, 52, 87]. For example, Hart et al.[52] used TGA-MS to monitor the dissociation process of H_2O and -OH on Ti_3CNT_x (Fig. 3). The first peak was attributed to H_2O loss, and thus the second peak was identified as -OH dissociation. Therefore, the onset was around 200 °C. Likewise, Zhou et al.[87] claimed that the -OH loss on Zr-based MXenes started from 200 °C. Differently, Kong et al.[51] used TGA-DSC to observe the thermal behavior of $Ti_3C_2T_x$ under N_2. There was an obvious mass loss around 400 °C and it was then attributed to -OH dissociation with the help of ^1H NMR.

However, regarding -F termination, the obtained dissociation behavior seems to vary drastically among papers using different characterization techniques. Based on XPS and/or EDX data, the atomic ratios of F/Ti and O/Ti on MXene surface can be achieved. The calculated ratios show that although

the onset of the -F dissociation is unknown, it starts to follow the footstep of -OH from as low as 200 °C[48, 50, 69]. The only difference is that the dissociation rate of -F is relatively slower than that of -OH[48, 69], a result of the aforementioned higher theoretical stability of -F than -OH. However, by combining TGA with either MS or DSC, an apparent -F loss onset can be achieved varying from 400 – 1000 °C or even higher, which is greater than the onset of -OH dissociation[51, 52, 88]. One assumption can be proposed to account for the contradiction: Although the major step of -F loss requires a higher temperature than -OH, it starts to dissociate slowly at low temperature like -OH. The apparent onset of -F dissociation demonstrated by MS cannot reveal the real behavior of -F since the background covers the weak signal. Supporting research was done by Seredych et al. [88]. As the concentration of -F increases (realized by increasing HF concentration in the etching process), they found that the apparent onset of -F dissociation moved to lower temperature (from c.a. 1000 °C to c.a. 400 °C, shown in Fig. 4), which is persuasive support for the above assumption.

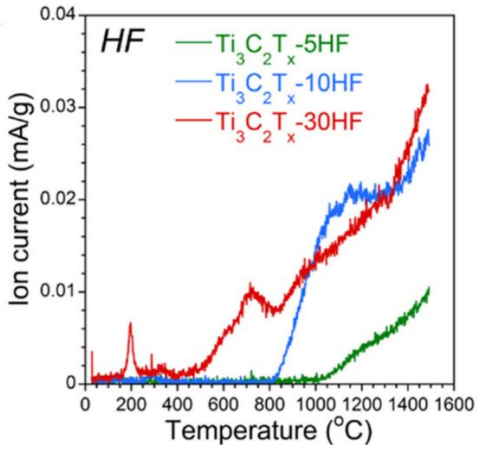

Fig. 4 MS analysis for the atomic mass unit of 20/HF. Reproduced with permission from ref. [88], Copyright © 2019 American Chemical Society.

For -O termination, resulting from its high stability, it can resist temperature as high as 750 °C or even higher[52, 86], where some $Ti_3C_2T_x$ samples are about to or have already degraded[48, 75, 88].

Consequently, no paper has specially dealt with the manipulation of -O termination as far as we know. The above-mentioned findings offer some opportunities to regulate the composition of surface terminations (like O/F ratio, O/Ti and F/Ti are used here to quantify the composition of surface terminations). For example, considering that the dissociation rate of -F is slower than that of -OH under relatively low temperature, Li et al.[69] successfully fabricated a type of F-rich Ti_2CT_x by eliminating oxygen-containing groups via annealing under 200 °C in a vacuum condition. After the heat treatment, the F/Ti (from 0.3 to 0.27) and O/Ti (from 0.16 to 0.037ratios) decreased, while the F/O ratio elevated from 1.83 to 7.26. As a result, the F-rich Ti_2CT_x demonstrated significantly small onset overpotential for hydrogen evolution reaction (75 vs. 265 mV for untreated Ti_2CT_x) and high exchange current density (412 vs. 40 $\mu A/m^2$ for untreated Ti_2CT_x). Based on the knowledge mentioned above that -F can be replaced by -OH in alkaline solution, Halim et al.[53] added an extra alkalization process before annealing. The result showed that the F/Ti of $Ti_3C_2T_x$ decreased from the initial 0.33 to 0.016 after the vacuum annealing under 550 °C for 1 h. Differently, the oxygen-containing species mostly retained on the surface in this case since they took up the preferred Ti sites during the alkalization process[86], thus becoming stabler than those introduced during the etching process. This stratagem could successfully increase the O/F ratio to 28. Although it was stated in this paper that the increased O/F ratio was seemingly not influential to the resistivity of $Ti_3C_2T_x$, the results confirmed the positive dependence of resistivity on the total amount of surface terminations reported by Wang et al. previously[75]. Alkalization could bring more surface terminations, while the heat treatment could reduce the amount of them. Therefore, by deliberately designing these two processes, one can nicely control the specific surface terminations and hence, control the resistivity of $Ti_3C_2T_x$ to the either higher or lower directions.

In the g-C_3N_4/$Ti_3C_2T_x$ composites, $Ti_3C_2T_x$ MXene with an oxygen terminated surface was

obtained by annealing the composites for one hour at 200 °C either in a tube furnace under N_2 protection or in a muffle oven in air[89]. The oxygen terminated $Ti_3C_2T_x$ acted as the cocatalyst for the photocatalytic hydrogen evolution reaction in the annealed g-C_3N_4/$Ti_3C_2T_x$ composites. The H_2 production of g-C_3N_4 with 30% Ti_3C_2 after annealing in air (10.9 μmol h^{-1} g_{cat}^{-1}) is 41% higher than that of the sample annealed in N_2 (7.8 μmol h^{-1} g_{cat}^{-1}) and 105% higher than that of the sample without annealing (5.3 μmol h^{-1} g_{cat}^{-1}). The enhanced H_2 production rate of the sample after annealing might be ascribe to the increased –O surface terminations on the Ti_3C_2 since more –O surface terminations can be generated after annealing in air than in N_2. For the g-C_3N_4/$Ti_3C_2T_x$ photocatalytic system, the –O surface terminations, which exhibited the lowest free energy of 0.011 eV with 25% coverages of atomic H, might be the active sites for the hydrogen evolution.

To remove all the terminations, the most frequently targeted species is -F. As discussed at the beginning of Section 2, it can be removed mainly before the degradation of MXenes, which makes it easier to remove when compared to -O. However, it is still not efficient enough to remove -F at low temperatures, which makes it a more worthwhile task when compared with -OH removal.

To realize the efficient removal of -F termination, annealing under an H_2-containing atmosphere was proved to be a reliable method[50, 90]. By annealing $Ti_3C_2T_x$ at 500 °C under a hydrogen atmosphere for merely 30 min, Lu et al.[50] reduced the F/Ti ratio from 0.2 to 0.05. Consequently, they improved the volumetric specific capacity of $Ti_3C_2T_x$ from ~56.3 to ~89.4 mA h cm^{-3} after 100 cycles (tested at 100 mA cm^{-3}). Likewise, Lai et al.[90] elevated the annealing temperature to 1100 °C (under Ar/H_2 atmosphere) and successfully eliminated almost all the -F groups on the surface of $Ti_2C(OH)_xF_y$. Moreover, since -OH was either removed or converted to -O, the surface was purely covered by -O, making $Ti_2C(OH)_xF_y$ eventually become Ti_2CO_x. As indicated in this paper, both $Ti_2C(OH)_xF_y$ and Ti_2CO_x demonstrated

semiconductor behaviors, but after the removal of -F, the resulted Ti_2CO_x demonstrated enlarged bandgap (80 meV) when compared with $Ti_2C(OH)_xF_y$ (10 meV). Therefore, the manipulation of surface termination is also a promising topic when it comes to the band structure engineering of semiconducting MXenes.

2.3 Regulation of surface termination by choosing different etching methods

As stated above, the original surface terminations are created during the etching process. Hence, the precursors involved and the reactions underwent will impact the composition of surface terminations of MXenes. By far, except for the aforementioned HF and LiF/HCl etching method, several other methods have been developed, including electrochemical etching[91-94], hydrothermal etching[67, 95], and molten salt etching[96-100]. Most of them are dedicated to developing an F-free etching process due to the inferior electrochemical performance caused by -F termination on MXenes. Therefore, more opportunities are offered for termination manipulation by regulating the etching process. However, since the impact of etching method to surface termination is quite a comprehensive topic, readers interested in this area are suggested to refer to some nice papers elsewhere[43, 101-104] that specifically cover this topic. Only the molten salt method is highlighted here due to its outstanding superiority in termination manipulation. Since the molten salt etching is a non-aqueous reaction process, it largely inhibits the unexpected side reactions like oxidation and hydrolysis[96], which means this method is much "cleaner" than the others. The proposed mechanism by Li et al.[97] is schematically shown in Fig. 5 for the etching process of $Ti_3C_2Cl_2$ by $ZnCl_2$.

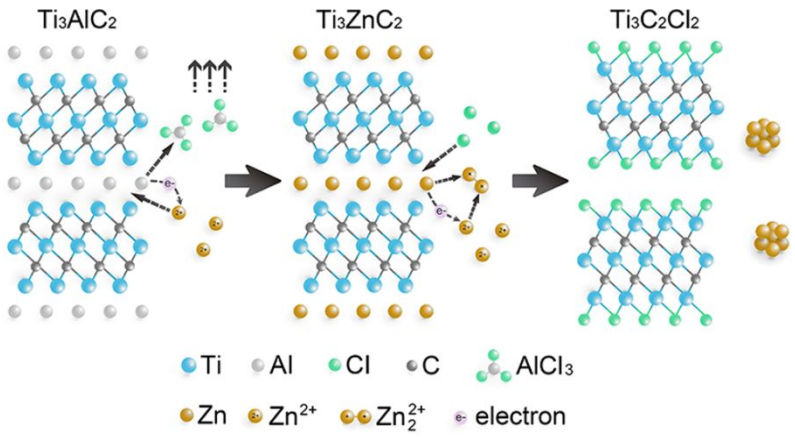

Fig. 5 Preparation mechanism of $Ti_3C_2Cl_2$ etched by $ZnCl_2$. Reproduced with permission from ref. [97], Copyright © 2019 American Chemical Society.

Usually, the etchants are transition metal halides such as $CdCl_2$[96], $CdBr_2$[96], $ZnCl_2$[97, 98], and $CuCl_2$[99, 100]. These transition metal halides can act as Lewis acidic species under molten salt state and, hence, can etch the A layer in the MAX phase. Since the anions involved here are halogens, the MXene produced via this method is terminated with halogen, different from the traditional methods.

Li et al.[97] demonstrated that when Ti_3AlC_2 reacts with molten $ZnCl_2$, it is initially transformed to Ti_3ZnC_2 and then etched to $Ti_3C_2Cl_2$ with Zn cluster and $AlCl_3$ gas being the by-products (Fig. 5). Therefore, the starting molar ratio of MAX/salt must play a critical role in this etching process. As they changed the ratio from 1:1 to 1:6, the final product gradually changed from Ti_3ZnC_2 to $Ti_3C_2Cl_2$. Theoretically, the resulting MXene should be terminated entirely by -Cl. However, a small amount of Ti-Cl was inevitably replaced by Ti-O during the washing process because the bonding effect of Ti-O was stronger than that of Ti-Cl[98]. Therefore, the Ti:Cl:O atomic ratio was 3:1.76:0.44 in the final product. It should be noticed that the residual $Al(OH)_3$ formed by the hydrolysis of $AlCl_3$ also contributed to the O composition. Therefore, the real O amount in the form of -O termination may be even lower. Again, attention should be paid to the washing of the as-prepared MXenes. Dong et al.[100] observed an even

more severe Cl-O substitution phenomenon after washing the exfoliated Nb_2CT_x with 0.5 M ammonium persulfate (APS) solution. The resulting composition was determined to be $Nb_2C_{1.11}O_{2.5}Cl_{0.25}$, implying that most of the -Cl was lost by APS washing and hence, the as-prepared MXene cannot be considered a Cl-terminated MXene.

Following this methodology, Li et al.[99] extended the MAX phase to Ti_3AlCN, Nb_2AlC, Ta_2AlC, and Ti_3SiC_2. With the help of thermodynamic calculation, they successfully etched these MAX phases to their corresponding MXenes by deliberately choosing salts such as $CdCl_2$, $FeCl_2$, $CoCl_2$, $CuCl_2$, AgCl, and $NiCl_2$, which demonstrated the superior universality of this method. By applying the optimal etchant, -Cl termination can be introduced to various MXenes. Furthermore, Kamysbayev et al.[96] creatively used $CdBr_2$ to prepare the Br-terminated MXenes ($Ti_3C_2Br_2$ and Ti_2CBr_2). Because the M-Br bond is weaker than the typical M-F and M-OH bond, the Br termination enables the ion exchange reaction on the surface of MXenes. By conducting the surface reaction under varied temperatures from 300 to 600 °C, they successfully prepared MXenes terminated by -NH, -S, -Se, and -Te. Specifically, they eliminated all the surface terminations by reacting $Ti_3C_2Br_2$ and Ti_2CBr_2 with LiH at 300 °C.

By far, only a few works reported the performances of the MXenes prepared by the molten salt method, probably a consequence of the early stage of this field. Li et al.[99] reported a Li-ion storage capacity of 205 mA h/g at 0.5 mV s^{-1} using a partially Cl-terminated MXene ($Ti_3C_{1.94}Cl_{0.77}O_{1.71}$). Dong et al.[100] used $Nb_2C_{1.11}O_{2.5}Cl_{0.25}$ to achieve a Li-ion storage capacity of 330 mA h/g at 0.05 A g^{-1}, which is incomparable with the alkalized MXene[79] results mentioned above. Kamysbayev et al.[96] observed the superconductivity of Nb_2CS_2, Nb_2CSe, and $Nb_2C(NH)$ under the low-temperature region (< 10 K), which suggests a promising application of the molten salt method in the manipulation of the superconducting property of MXenes.

By far, the molten salt method is still at its starting stage. Although the application of this method has not been well developed, it indeed offers a great possibility for the manipulation of various surface terminations.

Conclusively, this whole section introduced three methods that have been proved effective to manipulate the surface terminations of MXenes. The modification of the surface chemistry environment can lead to improved chemical and/or electrochemical performance, However, there is still a long way to go if a finely controlled manipulation process is desired.

3. Surface functionalization of MXenes

Although the original surface groups already have some impacts on the functionality of MXenes, surface functionalization with alien groups can bring even more features to the material. Owing to the abundance of original surface groups, the functionalization of MXenes is quite a facile process. The introduced molecules with functional groups can readily form either M-O-X bonding via reaction with -O and -OH[105-114] or direct M-X bonding by reaction with bare surface Ti atoms or replacing the surface groups[115-125] (X: the functional group or a molecule with a functional group, M: the metal element in MXenes). Armed with these functional groups, MXenes have demonstrated enhanced performance in fields where unfunctionalized MXenes can also be applied, such as environment material (dye adsorption[106, 107, 112] and ion adsorption[113, 114]) and energy material (supercapacitor[108, 119] and batteries[126]). Meanwhile, with the help of some functional groups, MXenes also demonstrated potential for broader applications, such as biosensor[109, 110] and anticancer therapy, which is usually a synergetic process combining several therapies like photothermal therapy, photodynamic therapy, and chemotherapy[116-118, 120-125].

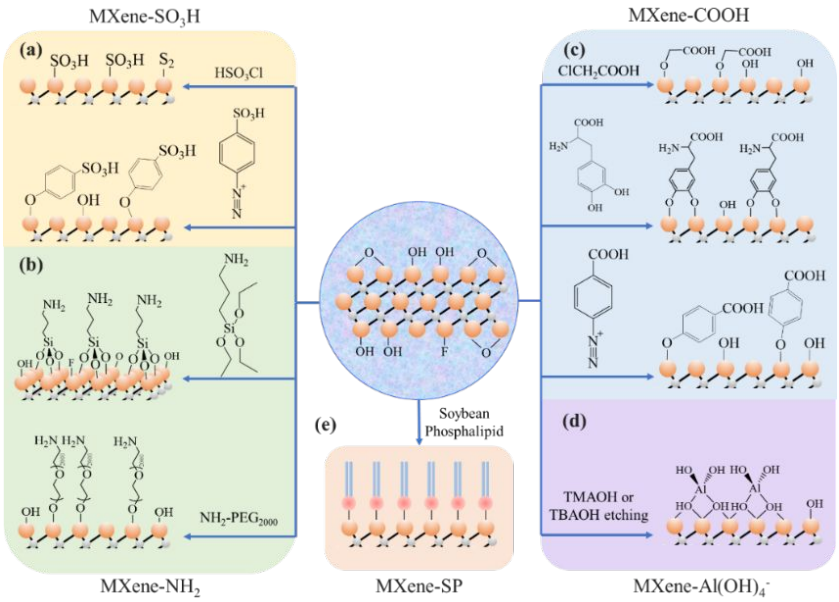

Fig. 6 A summary of five major surface functional groups and their bonding mechanisms on MXenes.

In this section, based on the actually effective units, five main types of surface functionalization over MXenes and their corresponding introducing mechanisms are schematically shown in Fig. 6, and the MXene surface functionalization and their corresponding applications were summarized in Table 2.

Table 2. Summary of MXene surface functionalization and their corresponding applications.

MXene	Functional groups	Precursor	Application	Performance	Ref.
$Ti_3C_2T_x$	-phenyl-SO_3H	Sulfanilic acid	-	-	105
$Ti_3C_2T_x$	-phenyl-SO_3H	Sulfanilic acid	Dye adsorption (MB)	Adsorption capacity improved from 21.10 to 111.11 mg/g after functionalization.	106
$Ti_3C_2T_x$	-phenyl-SO_3H	Sulfanilic acid	Dye adsorption (MB, RhB & ST)	Ordered aggregations were formed on the surface.	107
$Ti_3C_2T_x$	-phenyl-SO_3H	Sulfanilic acid	Supercapacitor	Specific capacitance improved from 69 to 160 F g^{-1} at 5 mV s^{-1} after functionalization.	108
$Ti_3C_2T_x$	-phenyl-SO_3H	Sulfanilic acid	Zn-ion battery	Functionalized $Ti_3C_2T_x$ provided higher Zn^{2+} diffusion coefficient, lower overvoltage, larger capacity, better rate capacity and better cycling stability.	126
$Ti_3C_2T_x$	-SO_3H	Chlorosulfonic acid	Magnetic material	-	115

$Ti_3C_2T_x$	-NH_2	APTES	Biosensor for CEA	Sensitivity: 37.9 μA ng^{-1} mL cm^{-2} per decade Detection range: 0.0001 – 2000 ng mL^{-1} Detection limit: 0.000018 ng mL^{-1}	109
$Ti_3C_2T_x$	-NH_2	APTES	Biosensor for CEA	Detection range: 0.001−1000 pM Detection limit: 0.15 fM	110
$Ti_3C_2T_x$	-NH_2	NH_2-PEG_{2000}	Photothermal therapy	21.1% cell viability *in vitro*, 200 ppm, 1.5 W cm^{-2}, 5 min Completely eradicated an *in vivo* tumor xenograft without reoccurrence.	111
$Ti_3C_2T_x$	-COOH	Chloroacetic acid	Dye adsorption (MB, ST & NR)	Maximum capacity of MB using Langmuir isotherm model: 81.9672 mg g^{-1} (298 K) 84.1751 mg g^{-1} (308 K) 86.2069 mg g^{-1} (318 K)	112
$Ti_3C_2T_x$	-COOH	Levodopa	Heavy metal ion adsorption (Cu)	Maximum capacity (pH = 11): 46.6 mg g^{-1} Removal efficiency (pH = 11): 93.2%	113
$Ti_3C_2T_x$	-COOH	4-aminobenzoic acid	Heavy metal ion adsorption (U & Eu)	Maximum adsorption capacities: U: 344.8 mg g^{-1} Eu: 97.1 mg g^{-1}	114
$Ti_3C_2T_x$	-$Al(OH)_4^-$	TMAOH	Photothermal therapy	α [a] : 29.1 L g^{-1} cm^{-1}	116
$Ti_3C_2T_x$	-$Al(OH)_4^-$	TMAOH	Photothermal therapy	α = 36.2 L g^{-1} cm^{-1}, η^b = 59.6%	125
$Ti_3C_2T_x$	-$Al(OH)_4^-$	TMAOH and $AlCl_3 \cdot 6H_2O$	Photothermal therapy	α = 28.6 L g^{-1} cm^{-1}, η = 58.3%	117
$Ti_3C_2T_x$	-$Al(OH)_4^-$	TBAOH	Photothermal therapy	α = 52.8 L g^{-1} cm^{-1}, η = 52.2%	118
$Ti_3C_2T_x$	-$Al(OH)_4^-$	TMAOH	Supercapacitor	Capacitance: 482 F g^{-1} (1 A g^{-1})	119
$Ti_3C_2T_x$	SP	SP	Photothermal Therapy	α = 25.2 L g^{-1} cm^{-1}, η = 30.6% The functionalized $Ti_3C_2T_x$ showed no noticeable toxicities either *in vitro* or *in vivo*	120
$Ta_4C_3T_x$	SP	SP	Photothermal therapy	α = 4.06 L g^{-1} cm^{-1}, η = 44.7%	121
$Ti_3C_2T_x$	SP	SP	Photothermal therapy	α = 5.0 L g^{-1} cm^{-1}, η = 22.9%	122
$Ta_4C_3T_x$	SP	SP	Photothermal therapy	α = 8.67 L g^{-1} cm^{-1}, η = 34.9%	123
$Ta_4C_3T_x$	SP	SP	Photothermal therapy	α = 4 L g^{-1} cm^{-1}, η = 32.5%	124
$Ti_3C_2T_x$	PFDTMS	PFDTMS	Solar desalination	Solar evaporation rate: 1.31 kg m^{-2} h^{-1} Solar steam conversion efficiency: 71% Stable under one sun over 200 hours	127

α: mass extinction coefficient

η: photothermal conversion efficiency

3.1 Phenylsulfonic group & sulfonic group (-SO_3H)

Usually, the denotation "-SO_3H" usually stands for both the phenylsulfonic and the sulfonic groups. However, due to its extra phenyl part, the phenylsulfonic group demonstrates more versatile functionalities than sulfonic groups and is more frequently used. The sulfonic group is proved to be highly active to donate proton[126], which can provide MXenes with more active sites. The phenyl group is also reported to produce extra active sites during electrochemical reactions[108]. Meanwhile, the phenylsulfonic group, as a whole, is negatively charged, which is beneficial to improve the electromagnetic force between MXenes and positively charged dye ions[106, 107]. Phenylsulfonic groups were introduced onto MXenes via aryl diazonium salt chemistry[105-108, 126] (Fig. 6a), which was proved to be an effective method to introduce foreign species to the surface of carbon-based material[128, 129] and metal nanoparticles[130]. A proposed reaction pathway is schematically illustrated later in this review (Section 3.3) for a similar reaction. Due to the metal carbide nature of MXenes, it was reasonable to introduce this method to the MXene field. The idea was firstly brought to this field as a novel way to delaminate $Ti_3C_2T_x$ in large-scale[105], then extended to chemical adsorption[106, 107], electrical material[108, 126], and magnetic material[115]. Apart from the commonly used method, sulfonic groups can also be directly grafted by chlorosulfonic acid (CS)[115] (Fig. 6a), which was known as a useful tool to introduce sulfonic groups to TiO_2[131, 132].

MXene materials have suffered from the low yield of delaminated flakes since its discovery[133] due to the high surface free energy[105]. Therefore, Wang et al.[105] creatively introduced phenylsulfonic groups to the surface to $Ti_3C_2T_x$, using Na^+ as prior interlayer spacer. Due to the larger size, phenylsulfonic groups can expand the interlayer space and weaken the interaction between layers and hence, delaminate $Ti_3C_2T_x$ to a greater extent. This research opened more opportunities for MXene surface

functionalization.

Following this research, Lei et al.[106] and Chen et al.[107] started to focus on the organic dye adsorption performance of this phenylsulfonic-functionalized MXene. Lei et al.[106] found that the methylene blue (MB) adsorption capacity of Ti_3C_2–SO_3H could reach 111.11 mg/g while that of the raw material was only 21.10 mg/g. Chen et al.[107] carried out more comprehensive and fundamental research involving MB, Rhodamine B (RhB), and Safranine T (ST). They focused on the self-assembling behaviors of the absorbates on the surface of Ti_3C_2–SO_3H. Thanks to the weak intermolecular force between phenylsulfonic groups and dye molecules (electrostatic force, π-π interaction, and hydrogen bonding), all three dyes could form ordered aggregations on the surface of Ti_3C_2–SO_3H. They found that MB and RhB molecules formed both H-aggregation (face-to-face stacking[134]) and J-aggregation (head-to-tail stacking[134]) while ST molecules mainly formed H-aggregation.

Extended work on the phenylsulfonic-modified MXenes was performed by Wang et al.[108] and Scheibe et al. [115]. With the help of the high specific surface area of delaminated Ti_3C_2–SO_3H, Wang et al.[108] made use of the merits of the pioneer work[105] and successfully prepared an electrode exhibiting enhanced supercapacitor performance. The delaminated nanosheets allowed more exposed surface atoms to react with electrolyte, resulting in a specific capacitance (Cs) of 160 F g^{-1} at 5 mV s^{-1} while the Cs of the unfunctionalized electrode was just 69 F g^{-1} at the same rate.

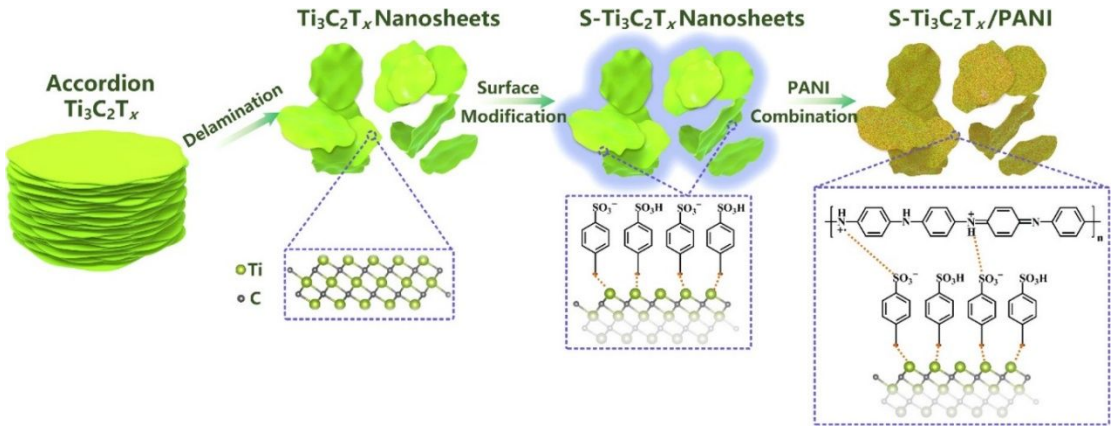

Fig. 7 Schematic of $Ti_3C_2T_x$ functionalization with phenylsulfonic group and the assembly with PANI. Reproduced with permission from ref. [126], Copyright © 2021 American Chemical Society.

Focused on the unique ability of sulfonic group to donate electron, Liu et al.[126] recently developed a new solution to stabilize polyaniline (PANI) on the surface of $Ti_3C_2T_x$ (shown in Fig. 7), which made this functionalized $Ti_3C_2T_x$ a promising candidate for Zn-ion battery (ZIB) cathode material. By grafting sulfonic groups in the form of phenylsulfonic groups to $Ti_3C_2T_x$ (via aryl diazonium salt chemistry), they successfully improved the protonation degree of PANI and inhibited its chronic deprotonation via providing continuous proton and locally high acidity. The improved protonation degree of PANI ultimately resulted in a high redox activity with good reversibility for the composite cathode material. Differently, Scheibe et al.[115] turned to inspect the magnetic properties of MXenes modified by sulfonic groups. They found that by partially substituting the original surface groups on HF-etched $Ti_3C_2T_x$ with sulfonic groups, the material started to exhibit mixed antiferromagnetic/paramagnetic behaviors under external magnetic field while the MAX phase and unfunctionalized $Ti_3C_2T_x$ demonstrated only paramagnetic behavior. Additionally, the functionalized $Ti_3C_2T_x$ exhibited two different types of radicals and/or defects in the electron paramagnetic spectrum.

3.2 Amino group (-NH_2)

In amino groups, the lone electron pair demonstrates versatile characteristics by forming coordination bonds with other groups or molecules. Therefore, they have been widely used as functional groups to endow absorbability[109, 110] or bridging joint[111] to construct composite. Chain molecules commonly graft it with two functional ends: one is -NH_2, and the other is for anchoring through reaction with original surface groups (Fig. 6b). Owing to the ultrathin 2D sheet-like morphology and excellent ion intercalation behavior, MXenes are ideal for electrochemical sensing after being loaded with

efficient surface sensing groups. Therefore, Kumar et al.[109] tried to introduce amino groups to the surface of single/few-layered $Ti_3C_2T_x$ in the form of (3-Aminopropyl) triethoxysilane (APTES) for biosensing (Fig. 6b – top panel & Fig. 8). The as-functionalized material demonstrated a wide linear detection range (0.0001–2000 ng mL^{-1}) and a low detection limit (0.000018 ng mL^{-1}) towards carcinoembryonic antigen (CEA, an important cancer biomarker) with high sensitivity (~ 37.9 μA ng^{-1} mL cm^{-2} per decade). The process was realized by the covalent immobilization of a bio-receptor (anti-CEA) on amino groups. Recently, following a similar procedure, Wu et al.[110] successfully introduced amino groups to a more complex MXene-based system to absorb anti-CEA.

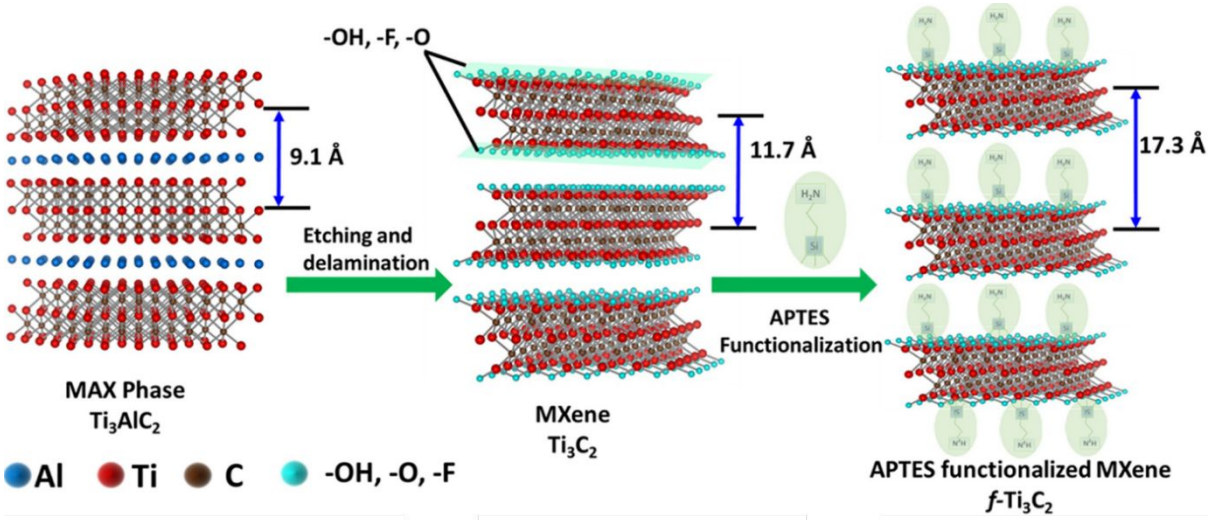

Fig. 8 Schematic of $Ti_3C_2T_x$ functionalization with APTES. Reproduced with permission from ref. [109], Copyright © 2018 Elsevier.

On the other hand, Zong et al.[111] used amino groups as a bridge to integrating GdW_{10} with $Ti_3C_2T_x$, aiming for both excellent photothermal reactivity and contrast-enhanced Computed Tomography (CT) and Magnetic Resonance Imaging (MRI). Amino groups were attached to the surface of $Ti_3C_2T_x$ by means of PEGylation using amino-(polyethylene glycol $(PEG)_{2000}$ (NH_2-PEG_{2000}) (Fig. 6b – bottom panel). The functionalized $Ti_3C_2T_x$ was then connected to -COOH groups on the surface of modified GdW_{10} by amide bonds. The resulting composite showed high photothermal ablation performance on

cancer cells (21.1% cell viability *in vitro*, 200 ppm, 1.5 W cm^{-2}, 5 min) and completely eradicated an *in vivo* tumor xenograft without reoccurrence.

3.3 Carboxyl group (-COOH)

Carboxyl groups have already been extensively inspected in graphene materials[135-137], owing to the similar surface chemistry environment, it is plausible to introduce carboxyl groups into MXene materials.[112-114] Similar to amino groups, carboxyl groups can be applied to a couple of chemicals via the aforementioned interaction with amino groups to form amide or ester[111, 112, 137]. Apart from the coupling reaction, carboxyl groups were also proven to adsorb metal ions by forming chemical bonds.[113, 114] Li et al.[112] transplanted the method previously used for graphene oxide (GO) functionalization[138] to the introduction of carboxyl groups to the surface to $Ti_3C_2T_x$, using chloroacetic acid as the precursor (Fig. 6c – top panel). By the interaction of carboxyl groups on MXene surface and amino groups in polyethylene polyimide (PEI), PEI was connected to MXene substrate for the deposition of poly (acrylic acid) (PAA). After layer-by-layer deposition of these two polymers, a core-shell structure could be constructed for dye adsorption, including ST, MB, and Neutral red (NR).

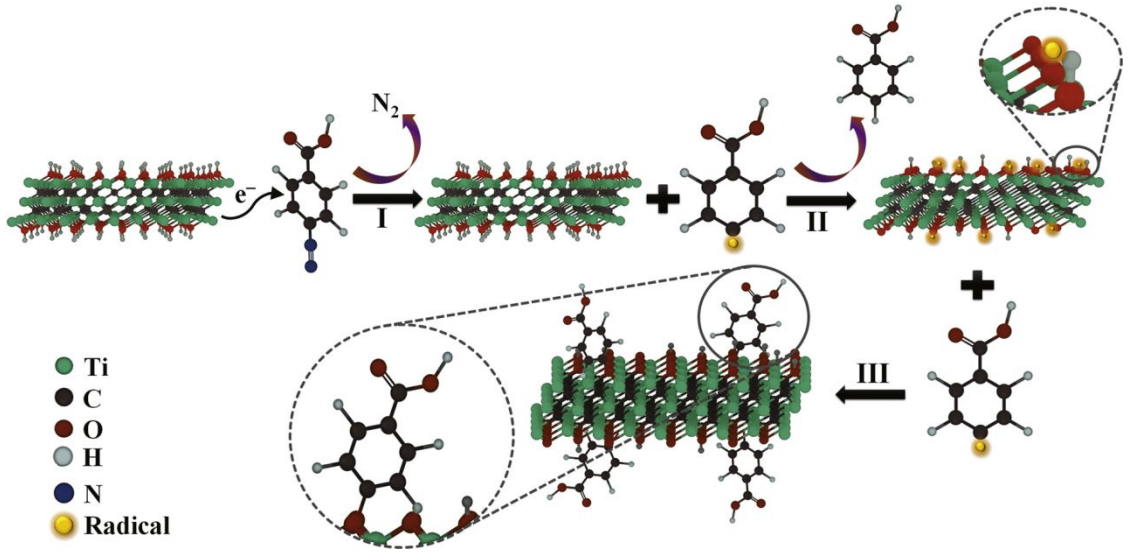

Fig. 9 Proposed reaction mechanism between $Ti_3C_2T_x$ and phenylcarboxylic acid diazonium salt. Reproduced with permission from ref. [114], Copyright © 2020 Elsevier.

Two additional contributions from Gan et al.[113] and Zhang et al.[114] exploited the interaction of heavy metal ions with carboxyl groups to realize chemical adsorption. Through "mussel-inspired chemistry", Gan et al.[113] successfully anchored Levodopa (DOPA), a kind of amino acid, by the interaction of its catechol groups with $Ti_3C_2T_x$ surface (Fig. 6c – middle panel). The decorated $Ti_3C_2T_x$ possessed abundant carboxyl groups and demonstrated efficient Cu^{2+} adsorption performance. Zhang et al.[114] took the diazonium salt chemistry route mentioned above using phenylcarboxylic acid diazonium salt as the intermediate to introduce carboxyl groups in the form of phenylcarboxylic acid (Fig. 6c – bottom panel). A proposed reaction pathway of this diazonium salt chemistry is shown in Fig. 9. As concluded in the paper, UO_2^{2+} and Eu^{3+} ions were mainly coordinated with the carboxyl groups by forming O-U and O-Eu bonds, respectively. The exhibited maximum adsorption capacities of the as-prepared material for U and Eu were 344.8 and 97.1 mg g^{-1}, respectively. As a comparison, the unfunctionalized $Ti_3C_2T_x$ demonstrated much lower capacities for both elements: 26 mg g^{-1} for U[139] and 54.05 mg g^{-1} for Eu[140].

3.4 Al oxoanion [-$Al(OH)_4^-$]

MXenes with -$Al(OH)_4^-$ termination were first introduced by Xuan et al.[116] via an organic reaction (Fig. 6d). Surprisingly, this surface group was found helpful for enhancing the localized surface plasmon resonance (LSPR) effect[116] of $Ti_3C_2T_x$, hence, enhancing the light absorption of $Ti_3C_2T_x$ in the near-infrared (NIR) region. The absorption in this region can result in heat generation, therefore, this functionalization can enhance the photothermal performance of $Ti_3C_2T_x$. Usually, this energy transformation process is depicted by two parameters: 1) mass extinction coefficient (α), which means how strongly a given mass of material absorbs light at a given wavelength, and 2) photothermal

conversion efficiency (η), which means how efficiently the material can convert the absorbed light into heat.

Other research groups[117-119] have optimized the method to afford to a greener and more efficient procedure to introduce $Al(OH)_4^-$ termination for MXenes. The originality of Xuan's research was the change of etchant for the MAX phase[116]. Based on the amphoteric nature of Al, they chose an organic base, tetramethylammonium hydroxide (TMAOH), instead of the traditionally used concentrated HF or LiF/HCl mixture, which are corrosive and unfriendly to the environment. The chemical process is schematically shown in Fig. 10. OH^- in TMAOH could attack Al atoms more efficiently, forming $Al(OH)_4^-$ in the solution environment. The resulting $Al(OH)_4^-$ was then attracted to the surface and bonded with Ti atoms of $Ti_3C_2T_x$. After the introduction of $Al(OH)_4^-$, $Ti_3C_2T_x$ demonstrated a strong and broad absorption in the NIR region, which improved the photothermal reactivity of the material. As a result, under the irradiation of 808 nm laser, the mass extinction coefficient of this functionalized $Ti_3C_2T_x$ was detected as high as 29.1 L g^{-1} cm^{-1}, making it an ideal candidate for photothermal anticancer therapy. Afterwards, Bai et al.[125] followed a similar procedure to functionalize $Ti_3C_2T_x$ and built a multifunctional nanocomposite drug delivery system based on it. The obtained system demonstrated an even higher mass extinction coefficient than Xuan's work (36.2 L g^{-1} cm^{-1}) under an 808 nm laser illumination with a high photothermal conversion efficiency of 59.6%.

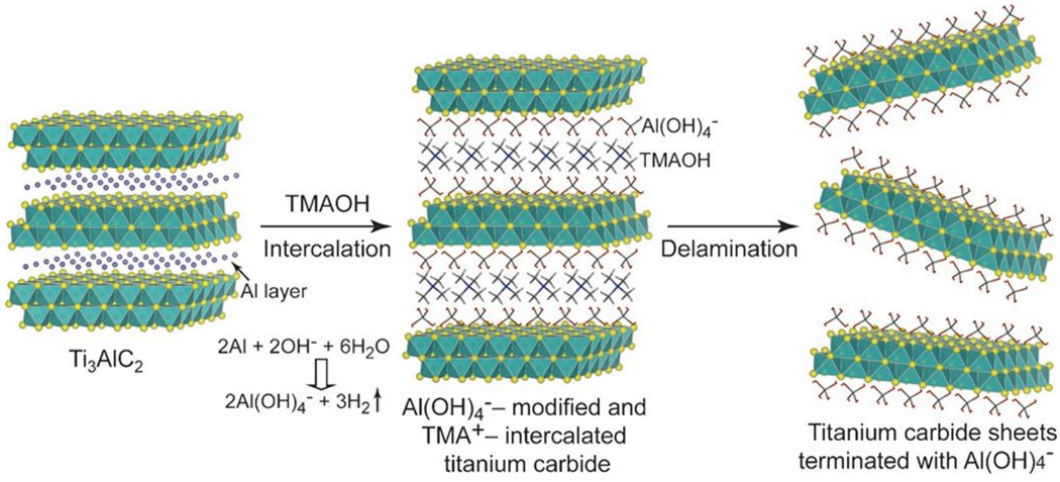

Fig. 10 Schematic illustration showing the intercalation and delamination process of $Ti_3C_2T_x$ using TMAOH. Reproduced with permission from ref. [116], Copyright © 2016 Wiley-VCH Verlag GmbH & Co. KGaA, Weinheim.

Then, Liu et al.[117] modified the etching process by supplying additive Al^{3+} (in the form of $AlCl_3 \cdot 6H_2O$) to avoid $Al(OH)_4^-$ loss during the long-term etching. Consequently, the functionalized $Ti_3C_2T_X$ nanosheets exhibited a high photothermal conversion efficiency of 58.3% under 808 nm irradiation. In the same year, Yu et al.[118] optimized Xuan's method by substituting TMAOH with tetrabutylammonium hydroxide (TBAOH) as the etchant, skipping the pretreatment step involving diluted HF solution[116]. Till then, the completely fluorine-free etching was realized. Moreover, the Florine-free surface drastically increased the mass extinction coefficient of the functionalized $Ti_3C_2T_x$ to 52.8 L g^{-1} cm^{-1} under 808 nm laser with a photothermal conversion efficiency of 52.2%. However, since the yield of single-layered MXenes was still very low (~ 20%)[119], Han et al.[119] focused on this blank area and successfully enhanced the yield to 74% through a hydrothermal-assisted intercalation (HAI) strategy (TMAOH was the etchant) instead of Xuan's intercalation and delamination two-step process. Consequently, the functionalized $Ti_3C_2T_x$ exhibited a capacitance of 482 F g^{-1} (at 1 A g^{-1}) higher than other reported data of MXenes and MXene-based materials[141-146].

3.5 Soybean phospholipid (SP)

As mentioned above, MXene-based materials have been widely used in photothermal therapy targeting tumor cells. However, the poor biocompatibility resulting from its instability in physiological solutions is still a big challenge. Regarding this problem, SP was then brought to this field without any apparent sacrifice of the photothermal property of MXenes[120-124] (Fig. 6e). SP is a complex mixture of various kinds of phospholipids, which is a family of amphiphilic organics composed of a hydrophilic head (red heads in the scheme) and hydrophobic acyl chains (blue tails in the scheme)[147] (Fig. 6e). Therefore, SP is a powerful tool to endow versatile solubility to MXenes, suitable for the physiologic environment. It was firstly grafted on $Ti_3C_2T_x$[120] and then extended to other MXenes[121] or MXene-based materials[122-124].

Lin et al.[120] introduced SP to the surface of $Ti_3C_2T_x$ through a "thin-film" approach, which is a type of chemical deposition. Via rotary evaporation of a mixture of precursors and solvents under vacuum, a thin film of SP can be coated onto $Ti_3C_2T_x$ with their hydrophilic heads attached to the $Ti_3C_2T_x$ surface. The resulting material was used for photothermal ablation of tumor (shown in Fig. 11) and no noticeable toxicity was shown in the test. Afterward, the same group[121] successfully grafted SP to the surface of $Ta_4C_3T_x$, a novel member in the MXene family. The prepared material demonstrated contrast-enhanced CT imaging property and higher photothermal conversion efficiency (from the previous 30.6%[120] to current 44.7% under 808 nm irradiation). Other contributions were made for contrast-enhanced CT and/or MRI via deposition of MnO_x[122, 123], or superparamagnetic iron oxide nanoparticles[124] on MXene surface. SP was involved in all these works as the surface modifier to enhance biocompatibility. However, it was clearly revealed in Table 2 that the α and η of the SP-functionalized MXene materials were incomparable to those of the MXenes functionalized by $-Al(OH)_4^-$, probably because of the

introduction of other materials onto MXene.

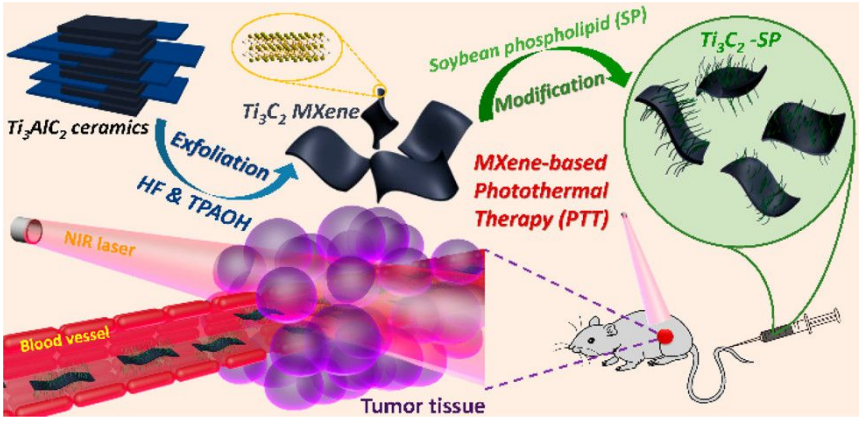

Fig. 11 Schematic of the fabrication process of SP-functionalized $Ti_3C_2T_x$ and the application of the material in photothermal therapy. Reproduced with permission from ref. [120], Copyright © 2016 American Chemical Society.

3.6 1H,1H,2H,2H-Perfluorodecyltriethoxysilane (PFDTMS)

In addition to the mostly reported functionalization as summarized in Fig. 6, the contacting angle on the MXene/water interface can be tuned by introducing different surface groups, switching MXenes between hydrophobic and hydrophilic applications. Inspired by the highly efficient photothermal conversion performance, Zhao et al.[127] deliberately designed a salt-blocking $Ti_3C_2T_x$ nanosheets membrane to split water from seawater under sunlight via distillation. A hydrophobic nature was required to prevent liquid water leakage and infiltration in membrane distillation. Therefore, the hydrophobicity was brought by them via PFDTMS functionalization. The reaction between O-CH_2CH_3 in PFDTMS and -OH group on the surface of $Ti_3C_2T_X$ can introduce hydrophobic groups to the surface of $Ti_3C_2T_x$[148].

In conclusion, surface functionalization is of great value to MXenes. By means of grafting different functional groups onto the surface, MXenes can be either enhanced in its electronic properties or introduced into the pharmacy field. Specially, as an important application of functionalized MXene, the

photothermal therapy using MXene has attracted a lot of research attentions. Some focused on the biocompatibility, grafting SP to make MXene a more ideal candidate for tumor treatment. Others focused on the enhancement of the photothermal effect. As stated above, SP-functionalized MXene demonstrated better biocompatibility while showing inferior photothermal performance to -$Al(OH)_4^-$ functionalized ones. Then it comes naturally that if more than one functional groups are introduced to MXene, it could make MXene possess multiple features simultaneously. Furthermore, following the same methodology reviewed above, more functional groups can be grafted onto MXenes, eventually making them more versatile materials.

4. Defect engineering of MXenes

Defects usually significantly affect the surface property of 2D materials, including MXenes[149-153]. Therefore, the detailed understanding of the ultrathin structure and defects is significant for shedding light on the physiochemical properties of the 2D materials. Defects have been studied in various 2D materials such as the MoS_2[154], WS_2[155], VSe_2[156], graphene[157], $NbSe_2$[158], and g-C_3N_4[159]. Defects can also be generated on MXenes during their preparation process and have exhibited a great effect on the property of the MXenes[160].

4.1 Generation of defects in MXenes

Among various defected MXenes, Ti_3C_2 MXene was the most widely studied. While oxygen vacancies can be formed through post-treatment with reducing gases, Ti defects, including the point defects and the defect clusters, can be formed during the etching process, and the defect concentration can be adjusted by altering the HF concentration[32, 161]. Moreover, the chemical property and electronic structure of the monolayer $Ti_3C_2T_x$ can be modified by the Ti defects on their surface[162]. Usually, the

defects are inclined to form on the top and bottom of the ultrathin MXene layer due to their direct contact with the etchant agent (e.g., HF). Based on the DFT simulation results, the defects are much easier to form in the outer Ti sublayer (formation energy: 2.842 eV) than in the inner Ti sublayer (formation energy: 6.485 eV)[161].

Etching conditions play an important role on the nature of the surface defect of MXenes. When LiF/HCl was used as the etching agent, the concentration and category of the surface defects were greatly affected by the etching time. For example, a shorter etching time result in less surface defects on the $Ti_3C_2T_x$[149]. Furthermore, the lateral size of the $Ti_3C_2T_x$ was destroyed with increasing etching time, increasing the roughness of the $Ti_3C_2T_x$ surface. And the point defects could be extended into line and 2D surface defects when the etching time was prolonged. In addition, the Ti atoms would be depleted during the prolonged etching time, and the C atoms left in the MXene spontaneously agglomerated into a carbon layer, which favors the formation of the graphitic carbon. In the meantime, the oxide was also inevitably generated during the etching process. In other words, high-quality MXenes with fewer defects can be obtained with less etching time. However, the Al cannot be removed entirely from the Ti_3AlC_2 to form the $Ti_3C_2T_x$ MXene when the etching time is not long enough.

In addition, the formation energy of the defects can be affected by the surface terminated functional groups. For example, the formation energy of Ti defects on the −O-terminated $Ti_3C_2T_x$ is much higher than that for bare Ti_3C_2, while the −F and –OH terminated $Ti_3C_2T_x$ exhibit comparable formation energy of Ti defects to that of bare Ti_3C_2[161, 163]. Similar results were obtained for the $Mo_2TiC_2T_x$ MXene[150]. The formation of Mo, Mo_2, MoTi, Mo_2Ti, and MoMo defects on the $Mo_2TiC_2T_x$ MXene terminated by oxygen is more energy consuming than that for the non-terminated MXene and the MXenes terminated by fluorine and hydroxide, which might be originated from the effect of the surface functions on the

bonding strength of the MXenes. On the surface of MXenes, O atoms share two electrons to form a covalent bond with the transition metals, while the F and O atoms make single and double bonds with the surface, respectively. Moreover, F and OH groups receive only one electron from the surface, indicating that O atoms make stronger bonds with the surface. Therefore, the binding strength between atoms is stiffer in the MXenes terminated by O atoms than those terminated by F or OH[150]. However, the relationship between the location of the defect and the surface termination or the effect of defects on the concentration of surface termination have not been investigated, and more efforts should be made in this field in the near future.

4.2 Effect of atomic defects on the electrical conductivity of MXenes

The structural quality and the electrical conductivity of MXenes can be controlled by tuning their surface Ti and C defects, and the electromagnetic interference attenuation ability of the MXene film can be influenced by the defect and the oxidative products. For instance, the electrical conductivity of the few-layer $Ti_3C_2T_x$ (f-$Ti_3C_2T_x$) membrane was significantly decreased with the increase of the etching time from 48 to 216 h, due to the increase in the Ti and C defects of f-$Ti_3C_2T_x$ with increased etching times[149]. In addition, the electromagnetic interference shielding effectiveness (EMI SE) performance of $Ti_3C_2T_x$ MXene film with lesser defects (31.97 dB) is better than that of the defected $Ti_3C_2T_x$ MXene (3.164 dB). Moreover, the $Ti_3C_2T_x$ MXene with lesser defects possesses abundant free electrons with high electron mobility. Therefore, most of the incoming EM waves were nullified by the highly oriented charge carriers via ohmic conduction loss (Fig. 12), and the EM waves were mostly reflected on the f-$Ti_3C_2T_x$. Moreover, the absorbed EM waves on f-$Ti_3C_2T_x$ vanished in the form of heat in the EMI shielding process. To sum up, the enhanced electromagnetic interference attenuation ability

of the MXenes can be obtained by controlling the density of defects and the structural quality of the MXenes in the preparation process.

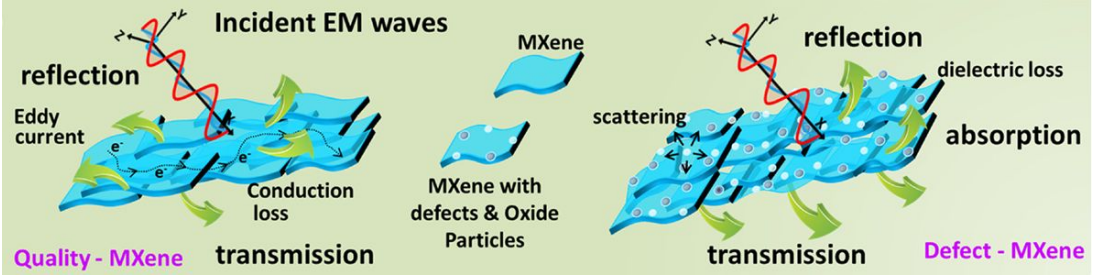

Fig. 12 Schematic illustration of EMI shielding for pure and defected f-$Ti_3C_2T_x$. Reproduced with permission from ref. [149], Copyright © 2020 American Chemical Society.

The oxygen vacancies can be increased on the MXene surface by post-processing with a reducing gas. The oxygen vacancies enriched $Ti_3C_2T_x$ flakes were prepared by reducing $Ti_3C_2T_x$ with H_2/Ar gas (H: $Ti_3C_2T_x$)[164]. Notably, due to the terminated -O and -OH groups on the $Ti_3C_2T_x$ surface, the carbon in $Ti_3C_2T_x$ is possible to be substituted by the oxygen of -O and -OH groups. Therefore, the elemental carbon species is possible to be generated, and part of the $Ti_3C_2T_x$ can be oxidized to TiO_2. The H:$Ti_3C_2T_x$ was combined with Cu_2O to form the composite photocathode by a dip-coating method for unassisted solar water splitting. The conductivity, light-harvesting efficiency, and charge-transfer ability of fabricated H:$Ti_3C_2T_x$/Cu_2O photocathode can be greatly enhanced by inducing the oxygen vacancies to the $Ti_3C_2T_x$. The H:$Ti_3C_2T_x$/Cu_2O photocathode displayed enhanced photoelectrochemical performance with a photocurrent density of −5.41 mA cm^{-2} at 0 V vs. RHE, which is 1.35, 1.26, and 1.22 times higher than that of Cu_2O, Au/Cu_2O and $Ti_3C_2T_x$/Cu_2O photocathodes, respectively. The exceptional performance of H:$Ti_3C_2T_x$/Cu_2O is ascribed to the enriched oxygen vacancies in the H:$Ti_3C_2T_x$ which can enhance the light-harvesting efficiency, conductivity, and charge-transfer ability

of the photocathode. Moreover, the result indicated that the $Ti_3C_2T_x$ is superior to noble metal Au for enhancing the photoelectrochemical performance of Cu_2O photocathode.

4.2 Effect of atomic defects on the ion diffusion in MXenes

Defects in MXenes can provide potential pathways for ion transport and diffusion. Titanium-deficient nitrogen-containing MXenes can also be used in potassium metal batteries. For example, the defect-rich and nitrogen-containing MXene (DN-MXene) exhibits potassium-philic characteristics and can induce the nucleation of K atoms, thus restraining dendritic growth during the plating/stripping process. The titanium-deficient nitrogen-containing MXene was coupled with carbon nanotubes (CNT) to obtain the DN-MXene/CNT scaffold, reducing local current density and promoting homogeneous K ionic flux attribute to the high electronic conductivity and fast K ion diffusion[165]. In addition, when the K@DN-MXene/CNT metal anodes were used in the K–S batteries, the matrix can protect the K metal from the shuttle effect of polysulfides by restraining the dendrite growth, which greatly enhances the electrochemical performances of the K–S batteries.

Structural holes can be created by partially etching the $Ti_3C_2T_x$ nanosheets with the H_2SO_4 oxidation as the etchant, and the etched $Ti_3C_2T_x$ nanosheets can be used to optimize the ion pathway in $Ti_3C_2T_x$ film for practical high-rate supercapacitor[166]. As shown in Fig. 13, nanometer-size holes/pores can be generated in the $Ti_3C_2T_x$ nanosheets after etching, while the crystal structure of $Ti_3C_2T_x$ around the holes was not changed, which indicated that the high electron conductivity and high pseudo capacitance of $Ti_3C_2T_x$ were retained. In addition, a few electrochemically inactive side-products, such as TiO_2, was generated on the $Ti_3C_2T_x$ surface. When the etched $Ti_3C_2T_x$ was used to form the $Ti_3C_2T_x$ film, the restacking issue was alleviated compared to the pristine $Ti_3C_2T_x$. Moreover, a hierarchical ion path “highway” in $Ti_3C_2T_x$ film can also be fabricated with atomic level increased interlayer spacing,

porous structure, and reduced flake size. Consequently, ultrahigh rate performance can be obtained with high volumetric capacitance.

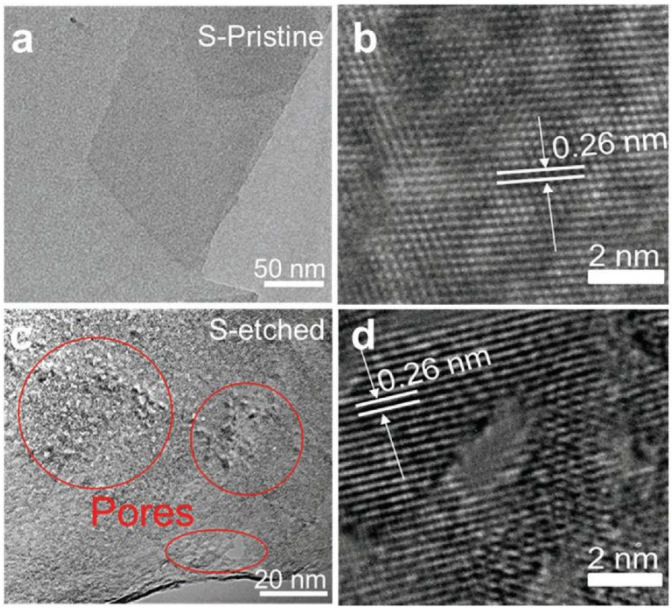

Fig. 13 Morphology and structure changes of $Ti_3C_2T_x$ nanosheets after etching. TEM images of (a,b) S-pristine and (c,d) S-etched $Ti_3C_2T_x$ nanosheets. Reproduced with permission from ref. [166], Copyright © 2020 Wiley-VCH GmbH.

4.3 Effect of atomic defects on the redox ability of MXenes

The surface defect engineering of MXenes exhibits a great effect on the electrical conductivity, electronic structure and redox ability[167, 168]. For example, Gogotsi et al.[169] reported that the monolayer $Ti_3C_2T_x$ MXene flakes with well-defined and clean edges and visually defect-free surfaces exhibited a field-effect electron mobility of 2.6 ± 0.7 $cm^2 V^{-1} s^{-1}$ and a low resistivity of 2.31 ± 0.57 μΩ·m (4600 ± 1100 S cm^{-1}). Chen et al.[170] used acid molecular (hydrofluoric acid) scissor to controllably tailor titanium atoms and obtain redox-active sites for pseudocapacitive reactions. During the tailoring process, the Ti vacancy can be formed in Ti_3CNT_x MXenes, and the atomic arrangement in the Ti_3CNT_x nanosheets became disordered. Moreover, three kinds of active nitrogens, such as Pyridinic-N,

Pyridinic-N-O and Pyrrolic-N, were generated after tailoring by hydrofluoric acid. These active nitrogens can supply additional negative charges via their lone electron pairs to adsorb electrolyte ions and further promote redox reactions, which will synergistically contribute to partial pseudocapacitance of Ti_3CNT_x. As a result, the tailored Ti_3CNT_x exhibits a significantly improved electrochemical performance with the specific capacitance reaching 376 F g^{-1} and 230.68 mF cm^{-2}, much higher than that of original Ti_3CNT_x (237 F g^{-1} and 168.27 mF cm^{-2}).

4.4 Effect of atomic defects on the surface adsorption property of MXenes

The surface adsorption property of MXene can be tuned by defect engineering[171]. For instance, the adsorption of N_2 molecules on the Ti_3C_2 can be enhanced by introducing Ti vacancy on the Ti_3C_2 surface[172]. The Ti vacancy induces a strong absorption energy for nitrogen atoms on the surface of BiOBr/Ti_3C_2 according to the DFT calculations, which enhanced the adsorption capacity of N_2 on the BiOBr/Ti_3C_2 composite catalyst. Moreover, the P-electron feedback caused by Ti vacancy could effectively promote the weakening of the N≡N triple bond and elongate the N_2 bond length by ~31.6%, thus facilitate the activation of N_2 molecules. With the 10 wt. % BiOBr/Ti_3C_2 composites as the catalyst for photocatalytic N_2 Fixation, the evolution rate of NH_3 is up to 234.6 μmol g^{-1} h^{-1}, which is approximately 48.8 times and 52.4 times higher than those of pure BiOBr and Ti_3C_2, respectively[172]. In addition, the Ti atom vacancy can also greatly improve the adsorption ability of $Ti_3C_2T_x$ to NO_2 and improved its detection sensitivity[173].

4.5 Challenges for the defect engineering of MXenes

The control of defect type and concentration in the preparation process of MXenes is quite challenging, especially in the etching process. Some progress has been made in introducing ordered defects in MXenes that can impact electrical conductivity. For example, 2D $Mo_{1.33}C$ MXene sheets with

ordered metal divacancy were prepared by selectively etching both Al and Sc from the 3D atomic laminate $(Mo_{2/3}Sc_{1/3})_2AlC$[174]. The 2D $Mo_{1.33}C$ with ordered metal divacancy shows 65% higher volumetric capacitance than Mo_2C with no vacancy at ~1,100 F cm^{-3}. Notably, the 2D $Mo_{1.33}C$ MXene flakes with ordered vacancies can be obtained in aqueous environments by the top-down method, and the yield is close to 100%[9], indicating that the MXene flakes can be prepared on a large scale. In general, a more effective and controllable strategy needs to be developed for the controllable preparation of the defected MXenes. Moreover, further efforts should be focused on revealing the property of the defected MXenes, which is essential for their practical application.

5. Metal/nonmetal doped MXenes

The defects on the surface of the MXenes are generally unstable and reactive. Therefore, MXenes were easy to be doped with metal or nonmetal atom, which will tremendously affect the physicochemical property of MXene.

5.1 Metal doped MXenes

When metal salt precursors are in contact with the surface of the defective MXenes, the metal cations can be reduced by the MXenes even without any additional reducing agent[175, 176]. Notably, the surface functional groups on the top and the bottom sublayer of the MXenes, such as O^{2-}, OH^-, and F^-, are beneficial to electrostatically adsorb the positively charged metal precursor, which is in favor of the subsequent reduction and the immobilization of the metal cations. Furthermore, the strong interaction between the metal atoms and the MXenes is conducive to the stability of the metal atoms and has a great effect on the electronic and chemical properties of the metal atoms[177]. In this case, the goal of maximized utilization of the noble metals can be achieved. For instance, Pt^{4+} in the $[PtCl_6]^{2-}$ complex ions can be reduced by the highly reductive Ti defects on the surface of $Ti_{3-x}C_2T_y$ at room temperature,

forming the $Pt_1/Ti_{3-x}C_2T_y$[162] whose electron microscopy image is shown in Fig. 14. Notably, the Pt atoms were stabilized in the Ti defects by substitution and formed strong Pt-C bonds, confirmed by the high-angle annular dark-field scanning transmission electron microscopy (HAADF−STEM) imaging and the extended X-ray absorption fine structure (EXAFS) analysis. Interestingly, only with a very small density of Pt (0.4 mmol %), the $Pt_1/Ti_{3-x}C_2T_y$ showed better catalytic performance than that of the commercial Pt catalysts and Pt nanoparticles (NPs) supported on $Ti_{3-x}C_2T_y$ for the N-formylation of CO_2 and aniline under ambient pressure.

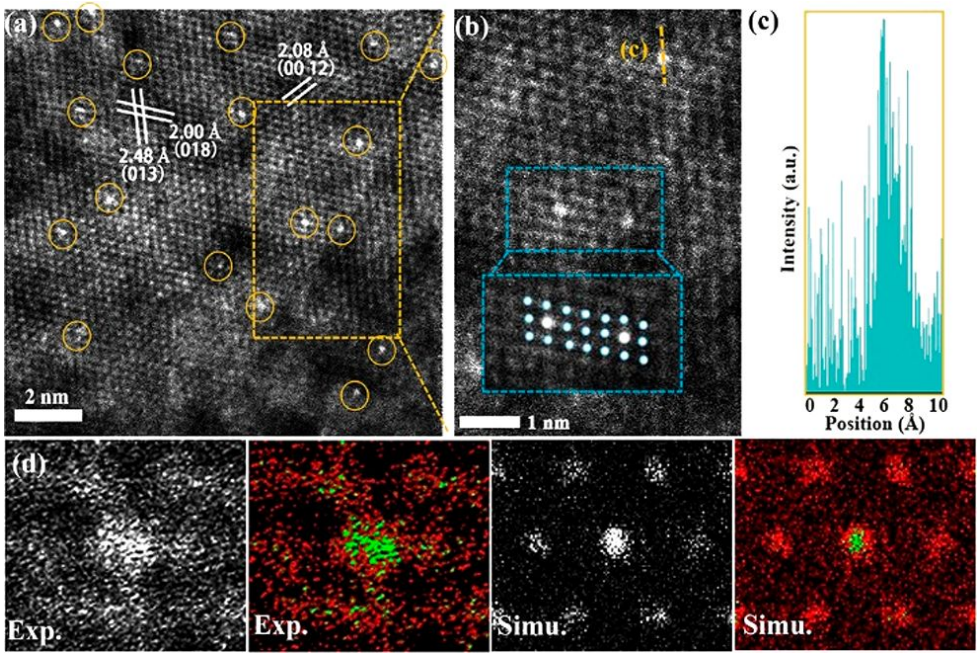

Fig. 14 (a) HAADF−STEM image of $Pt_1/Ti_{3-x}C_2T_y$. (b) Magnified HAADF image of the area in the yellow box in a. Schematic columns of atoms are overlaid on the experimental images (inset). (c) Corresponding intensity maps obtained in line 1 in b. (d) Experimental raw and falsely colored HAADF−STEM images (left two panels) and the simulated HAADF−STEM images (on the right) using a model with a Pt atom replacing one of the surface Ti atoms. Reproduced with permission from ref. [162], Copyright © 2019 American Chemical Society.

Except for Pt atom, Ru, Rh, Ir, and Pd can also be self-reduced in the Ti defects on the surface of MXenes[162, 178]. Ru^{3+} was directly reduced to Ru^0 on the Ti_3C_2 to form nanoconfined Ti_3C_2/Ru without any additional reductant. The resulting Ti_3C_2/Ru was used as the co-catalyst of TiO_2 for photocatalytic H_2 evolution[178]. During the reduction process of Ru, Ti_3C_2 was oxidized with the transformation of the Ti-OH surface group into Ti-O, which created a strong interaction between Ti_3C_2 and Ru. Ru was agglomerated into nanoclusters and dispersed on the Ti_3C_2 surface during the hydrothermal process, and the Ru^0 was not oxidized to RuO_2 after hydrothermal treatment, indicating its high stability. However, the interaction with Ti_3C_2 during the hydrothermal process caused a change in the work function of Ru, resulting in the low Fermi level of the Ti_3C_2/Ru system. When Ti_3C_2/Ru was used as the co-catalyst of TiO_2, the photogenerated electrons on the TiO_2 aggregated on Ti_3C_2/Ru could promote the H_2 production without any induction period. In addition, Ru can also be reduced on the Mo-deficit defect sites of the Mo_2CT_x MXene to form the Ru doped Mo_2CT_x[179]. The single-atomic Ru anchored on the defect sites of the Mo_2CT_x nanosheets acted as the electron back-donation centers for N_2 activation, promoting N_2 adsorption and activation and reducing the thermodynamic energy barrier of the first hydrogenation step. Therefore, the hydrogenation of the adsorbed N_2 was facilitated, promoting the formation of ammonia.

5.2 Nonmetal doped MXenes

In addition to metal doping, introducing surface vacancy and nonmetal dopant is also a feasible way to engineer the MXene surface. The Ti^{3+} species in $Ti_{3-x}C_2T_y$ MXene were verified as the intrinsic active sites for the electrocatalytic nitrogen reduction reaction, and the electronic state of the Ti^{3+} species can be tuned by vacancy and heteroatom doping[180]. For example, the surface Ti vacancies at the optimal level can trap the electrons, and the trapped electrons can be injected into an antibonding orbital of

adsorbed N_2 by the Ti^{3+}-N_2 dp π-back donation interactions, which promotes N_2 activation. In addition, the N-dopant species can not only minimize the orbits overlap between N_2 and Ti^{3+} and decrease the reaction energy barrier to facilitate the desorption of NH_3, but also act as the steady active sites for the nitrogen reduction reaction. Moreover, the activation barriers and kinetical desorption of NH_3 can be alleviated by optimizing the Ti vacancy density and N doping content in the $Ti_{3-x}C_2T_y$ MXene.

Sulfur (S) can be used as the mediator to modulate the surface chemistry and microstructure of MXenes. For example, Zhang et al. synthesized S-doped mesoporous $Ti_3C_2T_x$ films and used for the electrochemical sodium-ion storage (ESS). In the S-doped mesoporous $Ti_3C_2T_x$ films, S was doped into the $Ti_3C_2T_x$ structure by forming the Ti-S bond instead of the free elementary S. The Ti-S bond not only improves the electrolyte wettability, but also enhances the electrical conductivity of $Ti_3C_2T_x$. Moreover, the sulfur contents have great effect on the performance of the S-doped $Ti_3C_2T_x$ films. When the nominal sulfur to $Ti_3C_2T_x$ ratios was controlled to be 100% in the S-doped $Ti_3C_2T_x$ films (denoted as SMX-100), the electrical conductivities of the SMX-100 (2500 S cm^{-1}) was much higher than that of $Ti_3C_2T_x$ films (denoted as PMX, 625 S cm^{-1}). In addition, the initial reversible capacity of SMX-100 electrode (161.4 mAh g^{-1}) is higher than that of PMX (20.5 mAh g^{-1}), and the SMX-100 electrode exhibited decreased charge-transfer resistances (115 Ω) compared to that (371 Ω) of PMX, indicating the improvement of ion and electron transfer that results in the excellent sodium storage performances of SMX-100. However, S-doped $Ti_3C_2T_x$ films made from S/$Ti_3C_2T_x$ with higher S ratios such as 200% and 400% broke into pieces, which cannot be used directly as freestanding electrodes for ESS.

5.3 Challenges for metal/nonmetal doped MXenes

Metal/nonmetal doping on the defect sites of MXenes shows great potential in regulating and controlling the surface property of the MXenes. However, due to the difficulty in defect control (density

and structure) of MXenes, the precise metal/nonmetal doping on the MXene surface is very difficult. In addition, the stability of the doping heteroatom on the MXene surface needs to be improved for long-term use. Some heteroatom-doped MXenes were investigated by DFT calculation, while those heteroatom-doped MXenes were rarely reported experimentally. Therefore, more efforts are needed to exploit and utilize doped MXenes.

6. Surface oxidation of MXenes

MXenes are generally not stable under ambient conditions due to the collective effects from air, moisture, and light. For example, the surface of $Ti_3C_2T_x$ can be oxidized to TiO_2 at the atmospheric condition with water and oxygen, and the water molecules inserted between the MXene layers can accelerate the oxidation of the MXene.[181, 182] Such an oxidation of the MXene destroys the structural integrity and affects or changes the performance of the MXene flakes, such as the electrical properties, surface structure, and chemical constitution, which affect their potential applications.

6.1 Factors impacting the oxidation of MXenes

MXenes prepared by exfoliation methods are generally stored in deionized (DI) water due to their hydrophilic nature, and the MXene flakes easily form an aqueous colloidal suspension. However, MXenes are not stable in DI water because oxygen dissolved in DI water can oxidize MXenes into their oxidized forms.

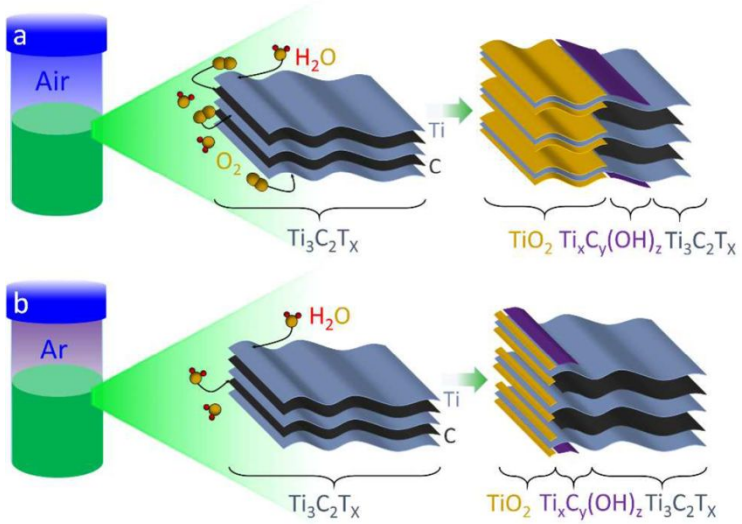

Fig. 15 Schematics of degradation of the colloidal d-$Ti_3C_2T_x$ MXene aqueous solution in (a) Air@RT and (b) Ar@RT. In panel a, the high solubility of oxygen in water provides a continuous source for MXene degradation. In panel b, in the absence of dissolved oxygen, water (a mild oxidant) slowly degrades the MXene flakes in the Ar-based environment. Reproduced with permission from ref. [183], Copyright © 2017, American Chemical Society.

Taking $Ti_3C_2T_x$, the most widely investigated MXene, as an example, when the $Ti_3C_2T_x$ aqueous colloidal solutions were stored in an open vial, the $Ti_3C_2T_x$ was degraded by 42%, 85%, and 100% after 5, 10, and 15 days, respectively, resulting in the formation of the oxide (mainly anatase TiO_2) colloidal solutions[183]. In the degradation process, the degradation of MXene starts at the edges, and the degradation kinetics follows a single exponential decay (Fig. 15a), and elevated temperatures can greatly accelerate the degradation process. The lateral size of the MXene also has a great effect on the degradation process. MXene flakes with smaller lateral size are less stable than those with larger size. Notably, the degradation of MXene colloidal solution can be suppressed substantially by removing the dissolved oxygen from water with Ar (Fig. 15b). However, the flakes still decay slowly over time due to the reaction between MXene and water (water is used as the mild oxidant) ($Ti_3C_2O_2$+4H_2O =

$3TiO_2+2C+4H_2$), and the $Ti_3C_2T_x$ could be degraded by 1.2% over 25 days.[183] To improve the stability of the MXene, separating MXene flakes from the water via vacuum-assisted filtration is considered an effective means because the compact morphology between the MXene layers prevents the inner MXene flakes from interacting with humid air[183].

To reveal the key factors responsible for the oxidation of MXenes in the aqueous solution, Mochalin et al. [184] studied the hydrolysis of two Ti-based MXenes. They found that the $Ti_3C_2T_x$ was still degraded in water in the oxygen-less atmosphere, which is in accord with the result obtained by Gogotsi et al. [183]. Over half of the $Ti_3C_2T_x$ was oxidized into TiO_2 over ~41 days in the water/Ar atmosphere. The degradation process of $Ti_3C_2T_x$ can be accelerated in the presence of O_2. Surprisingly, when the $Ti_3C_2T_x$ was preserved in the iso-propanol/O_2 environment, the time constant for degradation of $Ti_3C_2T_x$ was over 5 years. Therefore, it was concluded that water, rather than O_2, plays a critical role in the degradation reactions of the MXene, and it is water that MXenes should be protected from to improve their stability.[184] Yet, it is to be determined if this applies to other metal-based MXenes.

The formation of defects is usually unavoidable in the process of exfoliation of MXenes, and these defects have a great effect on the surface oxidation of MXenes. For example, the positive charged Ti-vacancies in Ti_3C_2 cause the C^{4-} to lose electrons and be oxidized, prompting amorphous carbon formation. Once the oxidation of MXene starts, the number and the size of pores become larger and larger, which promotes further oxidation[181]. Notably, the TiO_2 nanoparticles formed on the MXene surface are usually close to the pores formed by Ti-vacancies at the early oxidation stage. The edges, peaks, or valleys of wrinkles of the MXene are the sites for electron accumulation, and the Ti cations are more likely to be oxidized at these positions. Moreover, an internal electric field can be formed by the separation of electrons and holes, which promotes the Ti cations diffusion and the oxidation of the

MXene[181]. With time, MXenes are converted entirely into oxides. Therefore, it can be concluded that MXenes with fewer defects are more stable under environmental conditions.

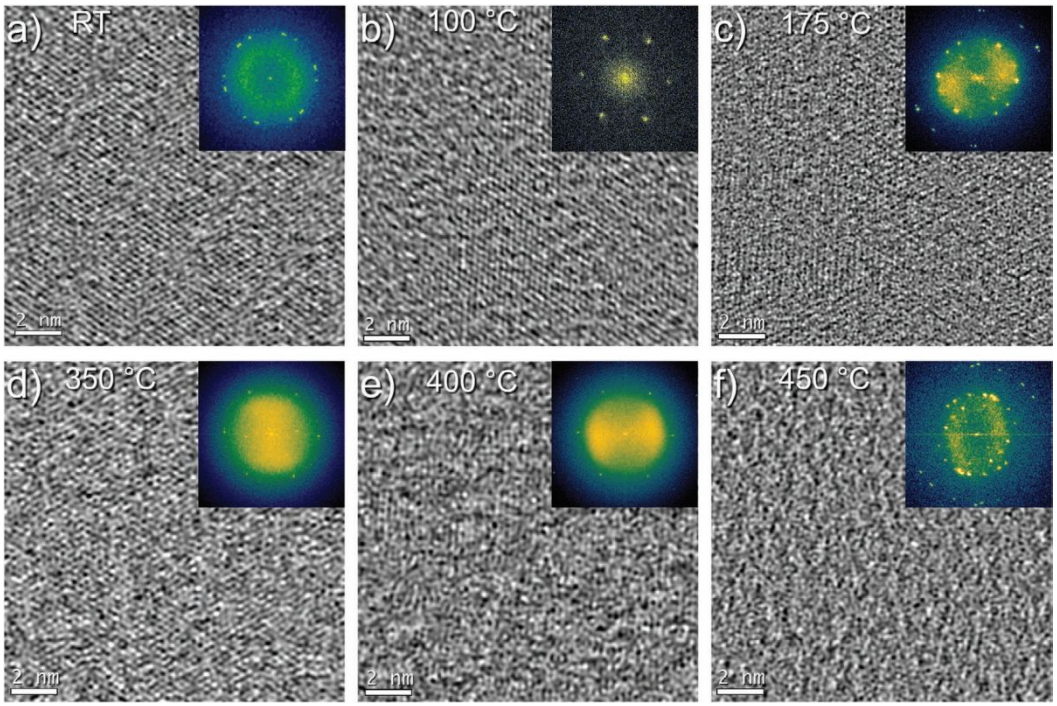

Fig. 16 Plan-view HRTEM images acquired from 1 to 3 $Ti_3C_2T_x$ stacked single flakes after exposure to 2 mbar O_2 gas for 0.5 h, at a) RT, b) 100 °C, c) 175 °C, d) 350 °C, e) 400 °C, and f) 450 °C. Insets show corresponding FFTs from a larger field of view (70 nm × 70 nm). Reproduced with permission from ref. [185], Copyright © 2020 The Authors. Published by WILEY-VCH Verlag GmbH & Co. KGaA, Weinheim.

It is an interesting question on how much oxygen the MXene surface can take before it breaks. To answer this question, Persson et al.[185] studied the oxidation of $Ti_3C_2T_x$ treated at different temperatures (100, 175, 350, 400, and 450 °C) in an oxygen environment. The surface of the $Ti_3C_2T_x$ is saturated by O at 100 °C ($Ti_3C_2O_x$, x = 2) and the oxygen content is relatively stable. When $Ti_3C_2T_x$ was exposed to oxygen at higher temperatures, the MXene structure was transformed into TiO_2 and released H_2O and CO_2 reaction products. According to the high resolution TEM (HRTEM) images of the oxidized $Ti_3C_2T_x$

(Fig. 16), a gradual increase in disorder can be observed from room temperature to 400 °C. The MXene lattice was barely visible from the HRTEM images after exposure of $Ti_3C_2T_x$ single sheets to O_2 at 400 °C, reaching a coverage of 1.74 O atoms per surface Ti atom ($Ti_3C_2O_x$, x = 3.48). Upon further increase to 450 °C, the MXene structure disappeared with the Ti:O content close to that of TiO_2. In this case, it can be concluded that the O terminations can reach supersaturation with $x \approx 3.5$ while the structure of the $Ti_3C_2T_x$ could be maintained.

The temperature and the heating rate greatly affect the oxidation process and the crystalline phase of the oxides on MXenes. For example, when Ti_3C_2 was placed in the presence of an oxidizing environment, flash oxidation (oxidation at higher temperatures for a short period of time – a few tens of seconds) leads to the formation of mainly anatase TiO_2 nanoparticles, while the rutile TiO_2 thin sheets can be obtained by slow heating over an extended period of time at lower temperatures[186]. The top and bottom Ti layers were first transformed into TiO_2, followed by the oxidation of the middle Ti layer. The oxidation of the carbon is also possible during the oxidation of Ti. However, Ti is preferentially oxidized due to the more negative Gibbs energy of Ti than that of the carbon. In this case, it usually forms the carbon supported TiO_2 after the oxidation of the Ti_3C_2 MXene.

6.2 Applications of oxidized MXenes

On a positive side, the oxidation of MXenes can be considered as a promising strategy to form MXene-based composites when the oxidation kinetics can be controlled. MXene-based composites, such as the combinations of MXenes with SnO_2[187], ZnO[188], Nb_2O_5[189], and TiO_2[190], have received a lot of attention in the fields of electromagnetic interference shielding, biomedical, optoelectronic, photocatalysis, and energy storage. For instance, the $Ti_3C_2T_x$ MXene films undergone a partially oxidation (obtained from the spontaneous oxidation of MXene flakes) showed strong photo response in

the ultraviolet region[23]. Furthermore, the relaxation process of photoexcited charge carriers takes a long time (~24 h), which makes the $Ti_3C_2T_x$ MXene films a potential material for photoresistors with memory effect for the application of optical detectors or comparators. In addition, the relaxation process can be greatly accelerated in the atmosphere containing oxygen and water vapor. This process is reversible, which renders the $Ti_3C_2T_x$ films attractive materials in the photo- and environmental sensing[23].

Gogotsi et. al[191] found that the oxidation of the MXene surface can be controlled by using CO_2 as a soft oxidant. We also synthesized Nb_2O_5/C/Nb_2C (MXene) composites by controlling the oxidation process of the Nb_2C surface with CO_2 as a mild oxidant[192]. The surface of the Nb_2C MXene was oxidized into Nb_2O_5 at 850 ^oC in the CO_2 atmosphere. In addition, the thickness of the Nb_2O_5 layer became thicker with the increasing of the oxidation time, and the molar ratios of Nb_2O_5/Nb_2C increased from 0.36 to 1.07 with the oxidation time from 0.5 to 1.5 h. With the controlled oxidation process, an intimate contact interface was formed between Nb_2O_5 and the conductive Nb_2C (Fig. 17), which is in favor of the separation of photo-generated charge carriers and enhanced the photocatalytic activity of water splitting. Notably, some amorphous carbon was also formed during the surface oxidation reaction, and the amorphous carbon is likely to function as a “binder” to maintain the structural integrity and the electron channel between Nb_2O_5 and Nb_2C.

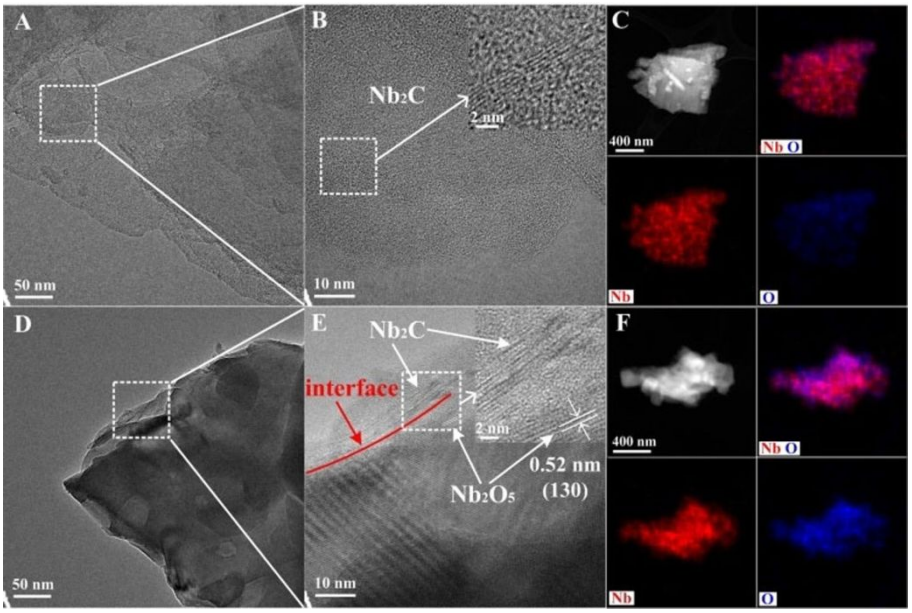

Fig. 17 TEM, HRTEM, and energy dispersive spectroscopy (EDS) analysis of (A–C) Nb_2C and (D–F) the oxidized Nb_2C. Reproduced with permission from ref. [192], Copyright © 2018 Wiley-VCH Verlag GmbH & Co. KGaA, Weinheim.

Due to the thermodynamically metastable transition metal atoms on the MXene surface, the transition metal atoms can be oxidized into metal oxide. For instance, oxygen-vacancy-rich TiO_2 nanoparticles can be *in situ* grown on the surface of $Ti_3C_2T_x$ nanosheets to form the $TiO_2/Ti_3C_2T_x$ composite by a one-step ethanol thermal treatment[193]. In this $TiO_2/Ti_3C_2T_x$ system, the oxygen vacancies of TiO_2 act as the main active sites for ammonia synthesis, and the highly conductive interior $Ti_3C_2T_x$ layers could not only promote the electron transport but also efficiently avoid the self-aggregation of the TiO_2 nanoparticles. In addition, due to the synergistic effects between TiO_2 and $Ti_3C_2T_x$, the $TiO_2/Ti_3C_2T_x$ catalyst exhibited higher electrocatalytic performance than that of pure $Ti_3C_2T_x$ and TiO_2 for the N_2 reduction reaction.

Partially oxidized MXene sheets can also be utilized for memory storage and electronic synapse applications. For example, partially oxidized $Ti_3C_2T_x$ sheets obtained by etching Ti_3AlC_2 at higher

temperature (65 °C) can be used for memristor with synapse and threshold resistive switching characteristics[194]. A small amount of TiO_2 particles was produced in the partially oxidized $Ti_3C_2T_x$ sheet, and these TiO_2 particles hampered the connections of $Ti_3C_2T_x$ sheets, hence the conductivity was almost close to that of an insulator. In addition, the partially oxidized $Ti_3C_2T_x$ sheets cannot have compact restacking with the TiO_2 particles on the surface act as the spacer, such spaces can provide a path for silver migration during the threshold switching. According to the threshold switching behaviors in $Ag/Ti_3C_2T_x$ NS/Pt device (NS denotes nanosheets) [194], the successive emulation of versatile synaptic functions, such as paired-pulse facilitation, post-tetanic potentiation, short-term potentiation, long-term potentiation, and transition from short-term potentiation to long-term potentiation memorization was demonstrated, which exhibited the promising application of MXenes in the field of the electronic devices.

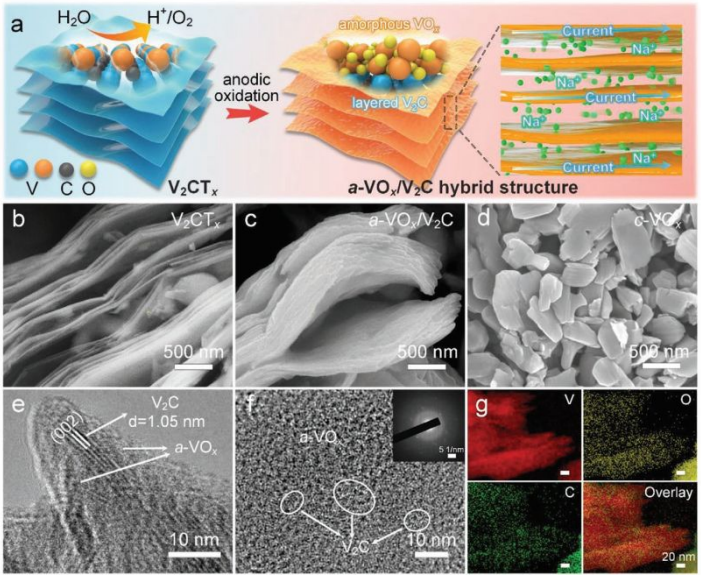

Fig. 18 (a) Schematic illustration showing the synthesis and structure of a-VO_x/V_2C nanohybrid. SEM images of (b) pristine V_2CT_x, (c) a-VO_x/V_2C, and (d) c-VO_x. (e, f) HRTEM images of a-VO_x/V_2C. The inset in (f) is the SAED pattern of a-VO_x/V_2C. (g) Elemental mapping of a-VO_x/V_2C. Reproduced with permission from ref. [195], Copyright © 2021 Wiley-VCH GmbH.

The surface of the V_2CT_x MXene is metastable and tends to be oxidized in water, and the a-VO_x/V_2C (a denotes amorphous) nanohybrid can be obtained by anodic oxidation at 1.8 V for 4 h in an aqueous electrolyte[195]. As can be observed in Fig. 18, V atoms in the outer surface of V_2CT_x can react with H_2O to form the amorphous and nanoscale VO_x layer, which was conformally coated on the V_2CT_x core. After the anodic oxidation, the surface of V_2CT_x becomes rougher due to the production of the nanometer a-VO_x layer, and the thickness of the VO_x layer is around 4–14 nm. When the a-VO_x/V_2C nanohybrid was used as a structured electrode, the amorphous and nanoscale VO_x layer can promote the diffusion of Na^+, provide a great deal of vacancies and active sites for Na^+ storage, and alleviate the corresponding volume changes simultaneously. In addition, the V_2C layer maintain the structural integrity of the electrode and acts as a conductive and robust skeleton for efficient ion/electron transport. Therefore, when the a-VO_x/V_2C composite acted as the cathode material for sodium-ion batteries, the a-VO_x/V_2C electrode exhibited high capacity, decent rate capability, and long-term cycling stability.

Oxidation of MXenes has also attracted attention in the field of photovoltaic devices, such as perovskite solar cells. The property of the electron transport layer (ETL) fabricated by $Ti_3C_2T_x$ can be tuned by the oxidation of the MXene[196]. The macroscopic defects of the film fabricated by spin-coating can be reduced by the oxidation of $Ti_3C_2T_x$ with the generation of the Ti–O bonds. Notably, the metallic material can be transformed into a semiconductor after heavy oxidation, resulting in a better matching of energy levels between the electron transport layers and perovskite, indicating the oxidized $Ti_3C_2T_x$ is more suitable as the ETLs for the perovskite solar cells. A power conversion efficiency (PCE) of 18.29% can be achieved for perovskite solar cells when composited with heavily oxidized $Ti_3C_2T_x$ as the ETL, which is higher than that (16.5%) of using pristine $Ti_3C_2T_x$ as the ETL. The enhanced PCE

can be ascribed to the increased electron mobility in the ETL and the reduced electron–hole recombination.

6.3 Oxidation Resistant MXenes

There are both advantages and disadvantages to the oxidation of MXenes. On the one hand, by controlling the oxidation degree of MXenes to synthesize the MXene-based composites, such as the MXene-based photocatalysts among others, the application of MXenes can be broadened. On the other hand, the oxidation of MXenes will reduce its stability, destroy the structural integrity, and decrease the electric properties, which will prevent their further commercial applications. Therefore, the oxidation of MXene should be controlled in some cases while be restrained in others. Various strategies have been developed by researchers to prevent the MXene from oxidation, as summarized in Table 3. In addition, a couple of typical antioxidant strategies for MXenes are discussed below.

It is a very practical way to store MXenes in a controlled environment to maintain their structural integrity. Contrary to high temperatures which can accelerate the oxidation of MXenes, lowering the temperature can slow down the oxidation of MXenes. Taking $Ti_3C_2T_x$ as an example, the resistance of $Ti_3C_2T_x$ sheets is kept constant for 39 weeks at -80 ^oC due to the low diffusion rate of the oxidants[182]. Because moisture is an accelerant to the oxidation reaction of MXenes, another valid way to improve the stability of MXenes is to store it in an anhydrous organic solvent, such as anhydrous ethanol or isopropyl alcohol. When MXenes are stored in organic solvent, the organic molecules are possible to adsorb on the surface or insert to the interlamination of the MXenes, which will inhibit the diffusion of gas molecules and gas adsorption. For example, when $Ti_3C_2T_x$ was stored in the anhydrous ethanol at 5 ^oC, the resistance of the MXene can be kept constant for 10 weeks[182].

Table 3. The antioxidant strategies for MXenes.

MXenes	Etching methods	Antioxidant strategies	Storage conditions	stabilization time	Refs.
$Ti_3C_2T_x$	LiF/HCl, RT, 24 h	lowering the Storage temperature	Air, water, -80 °C	39 weeks	182
$Ti_3C_2T_x$	LiF/HCl, RT, 24 h	stored in organic solvent	anhydrous ethanol, 5 °C	10 weeks	182
$Ti_3C_2T_x$	LiF/HCl, 35 °C, 24 h	cyclodextrin encapsulation method	water	500 h	197
$Ti_3C_2T_x$	LiF/HCl, 22 °C, 24 h	Plasmon-assisted MXene grafting with oleophilic -CF_3	nonpolar organic solvents	2 weeks	198
$Ti_3C_2T_x$	LiF/HCl, 20-23 °C, 36 h	proton acid colloidal processing approach	100% relative humidity environment	2 weeks	199
$Ti_3C_2T_x$	48% HF, RT, 8 h	storing in the deep eutectic solvents	urea:choline chloride or ethylene glycol:choline chloride	28 weeks	200
$Ti_3C_2T_x$	LiF/HCl, 35 °C, 24 h	bioencapsulation	water	22 days	201
$Ti_3C_2T_x$	LiF/HCl, 40 °C	Modification of MXene with Zn^{2+} ions and self-assembled with RGO	air, RT	60 days	202

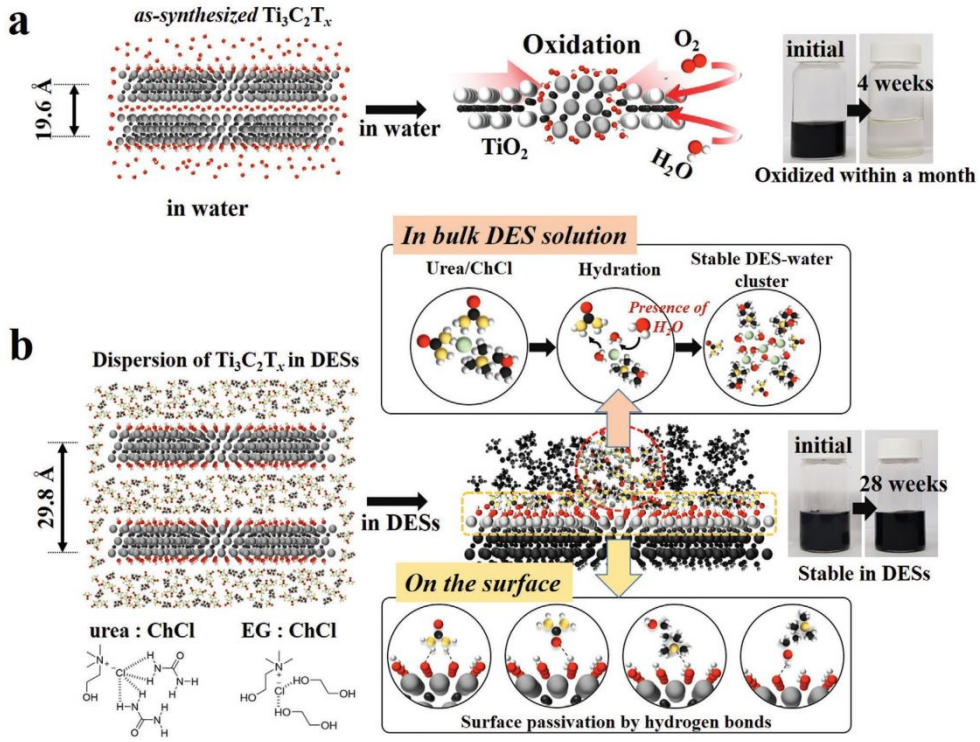

Fig. 19 Schematic illustration of the expected mechanism by which the oxidation of $Ti_3C_2T_x$ is prevented in DES dispersions. The $Ti_3C_2T_x$ dispersed in water (a) undergoes oxidation within a month, while that dispersed in a DES (b) shows long-term oxidation stability up to 28 weeks. Reproduced with permission from ref. [200], Copyright © 2021 Wiley-VCH GmbH.

Deep eutectic solvents (DESs) can also be used as an anti-oxidative dispersion medium for MXenes. For instance, the DESs, with the hydrogen bond accepting and donating molecules, can passivate the surface of the $Ti_3C_2T_x$ and prevent the oxidation reaction[200]. Fig. 19 shows a schematic illustration of the oxidation behavior of $Ti_3C_2T_x$. As shown in Fig. 19, the $Ti_3C_2T_x$ dispersed in water was oxidized within a month. However, when the $Ti_3C_2T_x$ was dispersed in the DESs, such as urea:choline chloride (urea:ChCl) and ethylene glycol:choline chloride (EG:ChCl), the $Ti_3C_2T_x$ did not show any obvious changes after storage for more than 28 weeks. The enhanced stability of $Ti_3C_2T_x$ in the DESs can be ascribed to the following reasons. The DES molecules adhere onto the surface of

$Ti_3C_2T_x$, and strong hydrogen bonds can be formed between each DES molecules and the functional groups on the $Ti_3C_2T_x$ surface. Therefore, the hydrogen bonding donor and acceptor, such as urea and ChCl, formed atomically thin passivation layer surrounding $Ti_3C_2T_x$ nanosheets, which preventing the oxidation reaction.

Removing the extrinsic intercalants in MXene film by proton acid colloidal processing approach is a feasible way to enhanced the stability of the MXene. For example, $Ti_3C_2T_x$ nanosheets processed with 0.1 M HCl exhibited enhanced conductivity, mechanical strength, and environmental stability compared with that of the untreated $Ti_3C_2T_x$[199]. This enhanced stability can be ascribed to the absence of extrinsic intercalants after proton acid processing, which makes $Ti_3C_2T_x$ films stable in humidity by blocking the intercalation of H_2O/O_2. Therefore, the conductance in $Ti_3C_2T_x$ films remained 79% of its original value after two weeks' storage in 100% RH environment, while the untreated $Ti_3C_2T_x$ films only remained 8% conductivity. In addition, the mechanical performance of the $Ti_3C_2T_x$ film obtained via proton acid-processing was also improved.

Modification of MXenes with Zn^{2+} ions and self-assembled with hydrophobic RGO nanosheets to form 3D porous MXene/graphene composite can enhance the stability of MXenes[202]. The 3D porous $Ti_3C_2T_x$/graphene composite with 5% RGO exhibited no obvious decay in electrical conductivity after 60 days. With the assistance of the sacrificial metallic Zinc template, the in situ produced Zn^{2+} ions destroy the electrostatic repulsive forces between $Ti_3C_2T_x$ nanosheets and act as crosslinking sites for the self-assembly of RGO nanosheets and $Ti_3C_2T_x$. Moreover, the oxygen-containing terminal groups on the $Ti_3C_2T_x$ surface and edge sites were reduced by metallic zinc powder as an antioxidant, and the in situ produced Zn^{2+} ions bonding with the hydroxy groups on $Ti_3C_2T_x$, which can remove the nucleation sites for TiO_2 nanoparticles and suppress the oxidation of the $Ti_3C_2T_x$. In addition, the

hydrophobic RGO connected with the $Ti_3C_2T_x$ can act as the shielding layers for preventing the surface of $Ti_3C_2T_x$ from exposing to oxygen and moisture. The above reasons account for the enhanced stability of the $Ti_3C_2T_x$.

7. Theoretical calculation of MXene surface engineering

In addition to experimental studies, theoretical simulations based on density functional theory (DFT) have also been extensively applied to understand MXene surface engineering in order to predict the properties of MXenes with different surfaces. When combined with experimental work, the theoretical studies can shed more comprehensive understanding of the physicochemical properties of MXenes and thus provide insights into the rational design of new promising MXene-based materials.

7.1 Prediction of defect formation

The formation of the surface defects and the property of the defective MXenes can be predicted by theoretical calculations. For example, DFT calculations indicated that the formation energy (0.6 ~ 2.7 eV) of carbon vacancy in Ti_2CT_2 MXene is lower than those of graphene while the migration energy is high[203]. Therefore, the carbon vacancies are thermodynamically stable on the MXene surface. Moreover, the electronic conduction and the stiffness of Ti_2CT_2 can be regulated by inducing the carbon vacancies. In addition, the carrier mobility of the Ti_2CO_2 can also be regulated by the O-Vacancy-line (OVL) defect[204]. More interestingly, the nonmagnetic Ti_2CO_2 MXene can be transformed into magnetic state by introducing the OVL defects.

Singh et al.[205] systematically screened the different types of atomic defects on the M_2X-type MXenes. They found that higher energy was required for the formation of $M_2C(V_{MC})$ and $M_2N(V_{MN})$ vacancies, while the formation of the $M_2C(V_C)$ and $M_2N(V_N)$ vacancies is preferable on M_2X-type MXenes, as shown in Fig. 20. In addition, the activation of CO_2 on the M_2X-type MXenes was also

investigated, and the M_2X-type MXenes from group III to VII series display superb CO_2 activation, especially group IV MXenes, such as Ti_2X and Zr_2X, which exhibit high adsorption energies and charge transfer from M_2X MXenes to CO_2. Moreover, the chemisorbed CO_2 can subsequently dissociate into CO and O species. The CO_2 capture, activation, and dissociation abilities of M_2X MXenes can be ascribed to the hybridization between π orbitals of CO_2 and d-orbitals of the metal sites in MXenes. Finally, they also proposed that charge transfer from MXenes to CO_2 is a better descriptor for quantifying CO_2 adsorption on MXenes than the work function.

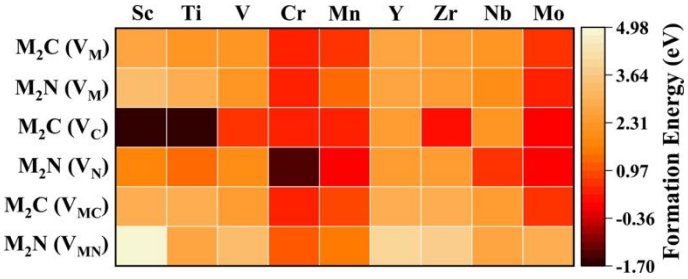

Fig. 20 Heatmap demonstrating the calculated vacancy formation energies of $M_2C(V_M)$, $M_2N(V_M)$, $M_2C(V_C)$, $M_2N(V_N)$, $M_2C(V_{MC})$, and$M_2N(V_{MN})$ systems. The vertical axis represents the studied vacancy systems, and the horizontal axis indicates the metal elements. Reproduced with permission from ref. [205], Copyright © 2021 American Chemical Society.

7.2 Prediction of the application of defected MXenes

The performance of 16 M_2XO_2-type MXenes (M=Ti, Zr, Hf, V, Nb, Ta, Mo, W, and X=C, N) with transition metal and carbon/nitrogen vacancies for the electrochemical carbon dioxide reduction reaction (CO_2RR) was investigated by the DFT[206]. Two kinds of adsorbates were formed on the M_2XO_2 surface, one is the –C-coordinated intermediates (e.g., *COOH and *CHO fragments), and another is the –H-coordinated intermediates (e.g., *HCOOH and *H_2CO complete molecules). The interaction between the –C-coordinated intermediates and MXenes can be enhanced by inducing the transition-

metal vacancies; while the interaction between the –H-coordinated intermediates and MXenes are largely unaffected. More importantly, the Fermi level of MXenes changes due to the formation of the vacancies, and the variation of Fermi level has a good linear relationship with the change of intermediate binding energy, which enables Fermi level shift to be an ideal descriptor to predict the catalytic activity of defective MXenes. Among 16 types of defective M_2XO_2, Hf_2NO_2 with Hf vacancies was regarded as the most promising defective MXene for CO_2RR[206]. The CO_2 adsorption on the defective $Mo_2TiC_2T_x$ was also studied by DFT, it was found that the CO_2 adsorption was enhanced by forming Mo defects in the monolayer $Mo_2TiC_2T_x$[150]. However, the CO_2 molecule cannot be activated due to the negligible charge transfer from MXene to CO_2, and thus the bond angle of the CO_2 is not significantly changed.

The conversion of CO into multi-carbon products is very challenging. Based on the DFT calculations, the defective $Mo_2TiC_2O_2$ MXene with dual-oxygen vacancy ($Mo_2TiC_2O_2$-$2O_V$) was considered as potential electrocatalysts for CO reduction into C_2 products[207]. The dual-oxygen vacancy on the $Mo_2TiC_2O_2$ surface can provide an appropriate environment to confine and enrich the active *COH species, which boosts the C–C coupling. Notably, the activation energy barrier of C–C coupling is lower than that on the copper surface. In addition, CO adsorption on the $Mo_2TiC_2O_2$-$2O_V$ surface is preferable than that of H_2O, which is beneficial for the reaction of CO reduction to ethanol rather than water reduction to hydrogen. Moreover, $Mo_2TiC_2O_2$-$2O_V$ exhibited higher electron density in the dual-oxygen vacancy, indicating that more electrons can be provided for the electrocatalytic CO reduction reaction. This work shows the potential of $Mo_2TiC_2O_2$-$2O_V$ as an efficient electrocatalyst for CO reduction.

Decorating the defective $Mo_{2-x}TiC_2O_y$ MXene with single transition metal (TM) atoms, such as Mo, Ru, Rh, W, Os, and Ir, is also a viable way to enhance the electrocatalytic performance of CO

reduction. However, the main product for the heteroatom-decorated $Mo_{2-x}TiC_2O_y$ MXene is CH_4[208]. In this heteroatom-decorated MXene system, the exposed TM–Mo–Mo triangle was regarded as the active site, the scaling relationship between CO reduction intermediates was broken by the surrounding oxygen atoms via the steric hindrance, as shown in Fig. 21. According to the DFT calculation, the W-decorated MXene was considered as the most promising CO reduction electrocatalyst, which exhibited a high selectivity for CH_4 production and strong suppression of the competing hydrogen evolution reaction.

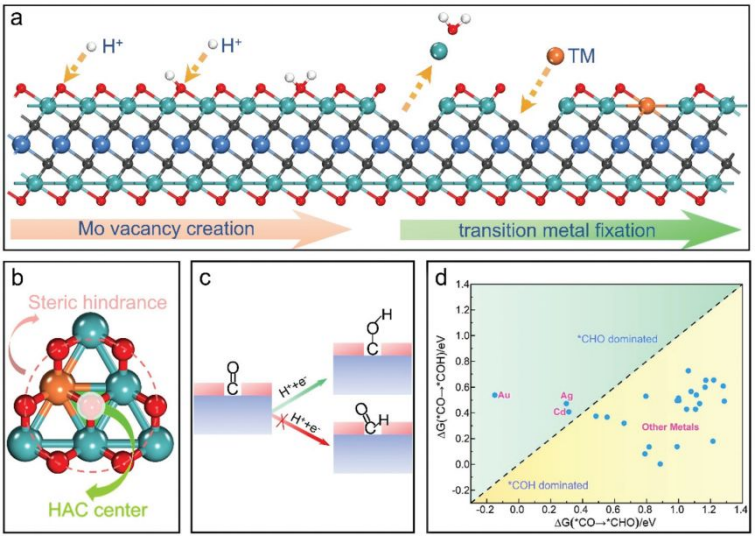

Fig. 21 (a) Schematic of the synthetic procedure of the transition metal-heteroatom catalyst (TM-HAC), where red, cyan, black, blue, white and saffron balls represent O, Mo, C, Ti, H and the embedded TM atoms, respectively. (b) Top view of the TM–Mo–Mo heteroatom active center, where the transparent red ball presents surface O-vacancy. (c) Scheme of the steric hindrance for the selective hydrogenation of *CO. (d) Comparison of the reaction free energies between ΔG(*CO → *CHO) and ΔG(*CO → *COH). Reproduced with permission from ref. [208], Copyright © 2020 The Royal Society of Chemistry.

The synergistic effect of surface vacancy and single transition metals on defective MXenes for nitrogen fixation was investigated by Jiang et al.[209] based on DFT calculation. For the transition metal

atom embedded $Ti_{3-x}C_2O_y$ MXene with surface Ti vacancies, 13 different transition metals (Ti, V, Cr, Mn, Fe, Co, Ni, Mo, Ru, Rh, Pd, W, and Pt) were examined. Only Mo or W supported on $Ti_{3-x}C_2O_y$ showed promising performance for the nitrogen reduction reaction (NRR), as the charges can be transferred between the adsorbed N_2 and the $Ti_{3-x}C_2O_y$ supports. Furthermore, the embedded transition metals can weaken the N≡N bond, strengthen the interaction between N_2 and the active site, and optimize the binding strength of key intermediate $*N_2H$. In $Ti_{2-x}C_2O_y$, Cr, Mo, and W were considered as the suitable transition metals. Among them, $W/Ti_{2-x}C_2O_y$ can greatly facilitate the NRR while restrain the competitive hydrogen evolution reaction, due to the synergistic effect of the exposed Ti atom and the transition metal atom around an extra oxygen vacancy.

Metal clusters can also be doped into the defective MXenes and have a great effect on the property of the MXenes. For example, Cu_3 cluster doped on the monolayer defect-free or defective Mo_2CO_2 surface was investigated by DFT[210]. In the presence of CO under reducing conditions, the Cu_3 active site was seriously damaged when it was doped on the surface of the defect-free Mo_2CO_2. On the contrary, when the Cu_3 cluster was doped on the O vacancies, formed by removing O atoms from pristine Mo_2CO_2, Cu_3 cannot be oxidized, and the Cu_3 doped Mo_2CO_2 showed superior performance toward CO oxidation. In the CO oxidation reaction, the Cu_3 cluster on the defective Mo_2CO_2 acted as an electron reservoir due to its electron-donating and -accepting ability. The doped Cu_3 cluster acted as an electron reservoir to attract the electrons from the defective Mo_2CO_2 before O_2 adsorption, while it donated electrons to O_2 after O_2 was adsorbed.

Theoretical calculation based on DFT is an effective way to predict the property of MXenes, which can guide the rational design of the MXene-based materials. The electronic structure, surface active site, gas adsorption, and defect formation energy can be investigated by the DFT calculation. In addition,

the performance of the MXenes in the application of CO oxidation, nitrogen fixation, and CO_2 reduction can also be predicted. However, there is a big gap between the theoretical calculations and the actual experimental environment. Thus, the result of the DFT calculation is for reference only. More experiment research needs to be carried out to verify the result of the theoretical calculation so that an experimental-computational feedback loop can be established.

8. Conclusions and prospect

In this review, we summarized the strategies for the surface engineering of MXenes, *i.e.,* the engineering of surface termination groups, surface functionalization, surface defects, surface doping, and surface oxidation. The impact of these surface engineering was also described on the performance of MXenes used in energy- and environment-related applications. Moreover, the theoretical simulations of surface engineering for the prediction of the properties of MXenes were also reviewed. The physicochemical properties, such as bandgap structure, electronic conductivity, flexibility, hydrophilicity/hydrophobicity, magnetism, metallicity, and stability, can be tuned by the surface engineering of the MXenes. Consequently, surface engineering is a practical way to obtain the desired properties of MXenes for their wide range of applications.

Despite a large body of work on surface engineering of MXenes in the past decade, there are still a lot of ambiguities about the precise surface control and the relationship between the surface states and the physicochemical properties of MXenes. Therefore, more dedicated work is still needed to shed more light on the surface engineering of MXenes.

Firstly, the current synthesis methods of MXenes are still rough and lead to MXenes with non-uniform surface structures/compositions. To etch the A element from the MAX phase, different kinds of etchants, such as the HF, LiF/HCl, and NH_4HF etc. have been used. The etching conditions have a

great effect on the surface structure of the resulting MXenes, such as the surface terminations, surface functional groups and defects. Therefore, it is hard to precisely control the concentration and the ratio of the surface terminations and defects by the wet chemical etching way. Moreover, some of the etchants such as HF are quite hazardous and need careful handling. Such a hazardous and less controllable method to obtain MXenes is not practical for the large-scale production of well-defined MXenes. Although there are some greener etching processes using organic bases like TMAOH and TBAOH, a functional layer of $-Al(OH)_4^-$ groups will be formed and the MXene is no longer a "pristine" material, which makes it difficult to do further surface manipulation of the MXene. Therefore, more effort should be invested into the development of safe, reliable, and tunable preparation methods, yielding high-quality MXenes with tunable surface properties. Specially, although the molten salt method is not a well-controlled process yet and still under development, it can completely avoid the usage of hazardous HF as well as introduce a variety of surface terminations to MXenes. Besides, the process is non-aqueous, which screens out the surface oxidation and hydrolysis, making it a "cleaner" process. In the near future, the molten salt method may become a competitive etching process owing to its iconic neatness, versatility, and benignity.

Secondly, the lack of systematic and fundamental study of the relationship between the surface terminations and manipulation parameters limits the development of surface engineering of MXenes. For example, surface alkalization and surface heat treatment are powerful tools when tailoring the amount and composition of surface terminations of MXenes. These processes are quite vulnerable to reaction parameters such as temperature and time. However, limited effort has taken a close look at these parameters. The lack of experimental guidance makes it impossible to finely manipulate the surface terminations.

Thirdly, the present surface characterization techniques are insufficient to comprehensively understand the surface characters of MXenes, which makes it very difficult to reveal the correlation between the surface character and the performance of the MXenes. For example, the metal vacancies can be directly observed using STEM, whereas the C/N and vacancies are very challenging to be investigated experimentally. Advanced characterization techniques are in great demand for surface characterizations, especially during the engineering processes of MXenes with *in situ* and *operando* techniques. In addition, the synergistic combination of experimental studies and theoretical simulations should be pursued to shed light on the relationship between surface engineering and the physicochemical properties of MXenes.

In summary, great achievements have been made on the surface engineering of the MXenes since their discovery about 10 years ago. Surface engineering has been demonstrated as a powerful approach to tailor the properties and functional performances of MXenes. Considering the large family of transition metal cations amendable for incorporation into MXenes, the structural and compositional spaces of MXenes with single and multiple metal cations are enormous. Combined with C, N and O as the X element, the surface chemistry of MXenes with tunable cations and anions is also boundless. Therefore, the vast opportunities are calling for the development of reliable and controllable surface engineering approaches to finely manipulate the rich physicochemical properties of MXenes and thus to further expand their applications in the fields of energy and environment as well as others.

Conflicts of interest

There are no conflicts to declare.

Acknowledgements

This work was supported by National Natural Science Foundation of China (22078074), Guangxi

Natural Science Foundation (2019GXNSFAA245006, 2020GXNSFDA297007), Opening Project of Guangxi Key Laboratory of Petrochemical Resource Processing and Process Intensification Technology (2021K009), Special funding for 'Guangxi Bagui Scholars', Scientific Research Foundation for High-level Personnel from Guangxi University. XM and ZW were supported by the Center for Nanophase Materials Sciences, which is a DOE Office of Science User Facility.

References

1. L. Lin, P. Sherrell, Y. Liu, W. Lei, S. Zhang, H. Zhang, G. G. Wallace and J. Chen, *Advanced Energy Materials*, 2020, **10**, 1903870.
2. Q. Wang and D. O'Hare, *Chemical Reviews*, 2012, **112**, 4124-4155.
3. U. Khan, P. May, A. O'Neill, A. P. Bell, E. Boussac, A. Martin, J. Semple and J. N. Coleman, *Nanoscale*, 2013, **5**, 581-587.
4. X. Xiao, H. Song, S. Lin, Y. Zhou, X. Zhan, Z. Hu, Q. Zhang, J. Sun, B. Yang, T. Li, L. Jiao, J. Zhou, J. Tang and Y. Gogotsi, *Nature Communications*, 2016, **7**, 11296.
5. X. Xiao, H. Yu, H. Jin, M. Wu, Y. Fang, J. Sun, Z. Hu, T. Li, J. Wu, L. Huang, Y. Gogotsi and J. Zhou, *ACS Nano*, 2017, **11**, 2180-2186.
6. F. Shahzad, A. Iqbal, H. Kim and C. M. Koo, *Advanced Materials*, 2020, **32**, 2002159.
7. M. Naguib, M. Kurtoglu, V. Presser, J. Lu, J. Niu, M. Heon, L. Hultman, Y. Gogotsi and M. W. Barsoum, *Advanced Materials*, 2011, **23**, 4248-4253.
8. Á. Morales-García, F. Calle-Vallejo and F. Illas, *ACS Catalysis*, 2020, **10**, 13487-13503.
9. A. Iqbal, P. Sambyal and C. M. Koo, *Advanced Functional Materials*, 2020, **30**, 2000883.
10. H. Xu, A. Ren, J. Wu and Z. Wang, *Advanced Functional Materials*, 2020, **30**, 2000907.
11. M. Hu, H. Zhang, T. Hu, B. Fan, X. Wang and Z. Li, *Chemical Society Reviews*, 2020, **49**, 6666-6693.
12. Y.-Z. Zhang, Y. Wang, Q. Jiang, J. K. El-Demellawi, H. Kim and H. N. Alshareef, *Advanced Materials*, 2020, **32**, 1908486.
13. V. M. Hong Ng, H. Huang, K. Zhou, P. S. Lee, W. Que, J. Z. Xu and L. B. Kong, *Journal of Materials Chemistry A*, 2017, **5**, 3039-3068.
14. F. Bu, M. M. Zagho, Y. Ibrahim, B. Ma, A. Elzatahry and D. Zhao, *Nano Today*, 2020, **30**, 100803.
15. L. Chen, K. Huang, Q. Xie, S. M. Lam, J. C. Sin, T. Su, H. Ji and Z. Qin, *Catalysis Science & Technology*, 2021, **11**, 1602-1614.
16. T. Su, Z. D. Hood, M. Naguib, L. Bai, S. Luo, C. M. Rouleau, I. N. Ivanov, H. Ji, Z. Qin and Z. Wu, *Nanoscale*, 2019, **11**, 8138-8149.
17. T. Su, Z. D. Hood, M. Naguib, L. Bai, S. Luo, C. M. Rouleau, I. N. Ivanov, H. Ji, Z. Qin and Z. Wu, *ACS Applied Energy Materials*, 2019, **2**, 4640-4651.
18. J. Halim, M. R. Lukatskaya, K. M. Cook, J. Lu, C. R. Smith, L.-Å. Näslund, S. J. May, L. Hultman, Y. Gogotsi, P. Eklund and M. W. Barsoum, *Chemistry of Materials*, 2014, **26**, 2374-2381.
19. M. Alhabeb, K. Maleski, B. Anasori, P. Lelyukh, L. Clark, S. Sin and Y. Gogotsi, *Chemistry of Materials*,

2017, **29**, 7633-7644.
20. Z. Kang, M. A. Khan, Y. Gong, R. Javed, Y. Xu, D. Ye, H. Zhao and J. Zhang, *Journal of Materials Chemistry A*, 2021, DOI: 10.1039/D0TA11735H.
21. L. Gao, W. Bao, A. V. Kuklin, S. Mei, H. Zhang and H. Ågren, *Advanced Materials*, **n/a**, 2004129.
22. C. Wang, S. Chen and L. Song, *Advanced Functional Materials*, 2020, **30**, 2000869.
23. S. Chertopalov and V. N. Mochalin, *ACS Nano*, 2018, **12**, 6109-6116.
24. M. Naguib, V. N. Mochalin, M. W. Barsoum and Y. Gogotsi, *Advanced Materials*, 2014, **26**, 992-1005.
25. R. M. Ronchi, J. T. Arantes and S. F. Santos, *Ceramics International*, 2019, **45**, 18167-18188.
26. L. Cheng, X. Li, H. Zhang and Q. Xiang, *The Journal of Physical Chemistry Letters*, 2019, **10**, 3488-3494.
27. T. Su, C. Men, L. Chen, B. Chu, X. Luo, H. Ji, J. Chen and Z. Qin, *Advanced Science*, 2022, **9**, 2103715.
28. A. Sinha, Dhanjai, H. Zhao, Y. Huang, X. Lu, J. Chen and R. Jain, *TrAC Trends in Analytical Chemistry*, 2018, **105**, 424-435.
29. Q. Jiang, Y. Lei, H. Liang, K. Xi, C. Xia and H. N. Alshareef, *Energy Storage Materials*, 2020, **27**, 78-95.
30. X. Zhang, Z. Zhang and Z. Zhou, *Journal of Energy Chemistry*, 2018, **27**, 73-85.
31. D. Xiong, X. Li, Z. Bai and S. Lu, *Small*, 2018, **14**, 1703419.
32. B. Anasori, M. R. Lukatskaya and Y. Gogotsi, *Nature Reviews Materials*, 2017, **2**, 16098.
33. N. K. Chaudhari, H. Jin, B. Kim, D. San Baek, S. H. Joo and K. Lee, *Journal of Materials Chemistry A*, 2017, **5**, 24564-24579.
34. S. Sun, C. Liao, A. M. Hafez, H. Zhu and S. Wu, *Chemical Engineering Journal*, 2018, **338**, 27-45.
35. R. Thakur, A. VahidMohammadi, J. Smith, M. Hoffman, J. Moncada, M. Beidaghi and C. A. Carrero, *ACS Catalysis*, 2020, **10**, 5124-5134.
36. J. Zhu, E. Ha, G. Zhao, Y. Zhou, D. Huang, G. Yue, L. Hu, N. Sun, Y. Wang, L. Y. S. Lee, C. Xu, K.-Y. Wong, D. Astruc and P. Zhao, *Coordination Chemistry Reviews*, 2017, **352**, 306-327.
37. J. Yang, W. Bao, P. Jaumaux, S. Zhang, C. Wang and G. Wang, *Advanced Materials Interfaces*, 2019, **6**, 1802004.
38. K. Huang, Z. Li, J. Lin, G. Han and P. Huang, *Chemical Society Reviews*, 2018, **47**, 5109-5124.
39. B.-M. Jun, S. Kim, J. Heo, C. M. Park, N. Her, M. Jang, Y. Huang, J. Han and Y. Yoon, *Nano Research*, 2019, **12**, 471-487.
40. J. Peng, X. Chen, W.-J. Ong, X. Zhao and N. Li, *Chem*, 2019, **5**, 18-50.
41. M. Naguib, M. Kurtoglu, V. Presser, J. Lu, J. Niu, M. Heon, L. Hultman, Y. Gogotsi and M. W. Barsoum, *Adv Mater*, 2011, **23**, 4248-4253.
42. O. Mashtalir, M. Naguib, V. N. Mochalin, Y. Dall'Agnese, M. Heon, M. W. Barsoum and Y. Gogotsi, *Nat Commun*, 2013, **4**, 1716.
43. M. A. Hope, A. C. Forse, K. J. Griffith, M. R. Lukatskaya, M. Ghidiu, Y. Gogotsi and C. P. Grey, *Phys Chem Chem Phys*, 2016, **18**, 5099-5102.
44. A. VahidMohammadi, J. Rosen and Y. Gogotsi, *Science*, 2021, **372**, eabf1581.
45. A. N. Enyashin and A. L. Ivanovskii, *Comput Theor Chem*, 2012, **989**, 27-32.
46. Y. Xie and P. R. C. Kent, *Phys Rev B*, 2013, **87**.
47. T. Li, X. Yan, L. Huang, J. Li, L. Yao, Q. Zhu, W. Wang, W. Abbas, R. Naz, J. Gu, Q. Liu, W. Zhang and D. Zhang, *Journal of Materials Chemistry A*, 2019, **7**, 14462-14465.
48. T. Yun, H. Kim, A. Iqbal, Y. S. Cho, G. S. Lee, M. K. Kim, S. J. Kim, D. Kim, Y. Gogotsi, S. O. Kim and C. M. Koo, *Adv Mater*, 2020, **32**, e1906769.

49. Q. Tang, Z. Zhou and P. W. Shen, *Journal of the American Chemical Society*, 2012, **134**, 16909-16916.
50. M. Lu, H. Li, W. Han, J. Chen, W. Shi, J. Wang, X.-M. Meng, J. Qi, H. Li, B. Zhang, W. Zhang and W. Zheng, *J Energy Chem*, 2019, **31**, 148-153.
51. F. Kong, X. He, Q. Liu, X. Qi, Y. Zheng, R. Wang and Y. Bai, *Electrochim Acta*, 2018, **265**, 140-150.
52. J. L. Hart, K. Hantanasirisakul, A. C. Lang, B. Anasori, D. Pinto, Y. Pivak, J. T. van Omme, S. J. May, Y. Gogotsi and M. L. Taheri, *Nat Commun*, 2019, **10**, 522.
53. J. Halim, I. Persson, P. Eklund, P. O. Å. Persson and J. Rosen, *Rsc Adv*, 2018, **8**, 36785-36790.
54. C. Eames and M. S. Islam, *Journal of the American Chemical Society*, 2014, **136**, 16270-16276.
55. Y. Xie, M. Naguib, V. N. Mochalin, M. W. Barsoum, Y. Gogotsi, X. Q. Yu, K. W. Nam, X. Q. Yang, A. I. Kolesnikov and P. R. C. Kent, *Journal of the American Chemical Society*, 2014, **136**, 6385-6394.
56. Y. Wang, C. Ma, W. Ma, W. Fan, Y. Sun, H. Yin, X. Shi, X. Liu and Y. Ding, *2D Materials*, 2019, **6**.
57. Z. Wei, Z. Peigen, T. Wubian, Q. Xia, Z. Yamei and S. ZhengMing, *Materials Chemistry and Physics*, 2018, **206**, 270-276.
58. X. Zhu, B. Liu, H. Hou, Z. Huang, K. M. Zeinu, L. Huang, X. Yuan, D. Guo, J. Hu and J. Yang, *Electrochim Acta*, 2017, **248**, 46-57.
59. S. Li, L. Wang, J. Peng, M. Zhai and W. Shi, *Chem Eng J*, 2019, **366**, 192-199.
60. L. Wang, H. Song, L. Yuan, Z. Li, Y. Zhang, J. K. Gibson, L. Zheng, Z. Chai and W. Shi, *Environ Sci Technol*, 2018, **52**, 10748-10756.
61. J. Guo, Q. Peng, H. Fu, G. Zou and Q. Zhang, *The Journal of Physical Chemistry C*, 2015, **119**, 20923-20930.
62. W. Mu, S. Du, Q. Yu, X. Li, H. Wei and Y. Yang, *Dalton Trans*, 2018, **47**, 8375-8381.
63. L. Wang, W. Tao, L. Yuan, Z. Liu, Q. Huang, Z. Chai, J. K. Gibson and W. Shi, *Chem Commun (Camb)*, 2017, **53**, 12084-12087.
64. Q. Peng, J. Guo, Q. Zhang, J. Xiang, B. Liu, A. Zhou, R. Liu and Y. Tian, *J Am Chem Soc*, 2014, **136**, 4113-4116.
65. Y. Dall'Agnese, M. R. Lukatskaya, K. M. Cook, P.-L. Taberna, Y. Gogotsi and P. Simon, *Electrochemistry Communications*, 2014, **48**, 118-122.
66. S. Yang, P. Zhang, F. Wang, A. G. Ricciardulli, M. R. Lohe, P. W. M. Blom and X. Feng, *Angew Chem Int Ed Engl*, 2018, **57**, 15491-15495.
67. T. Li, L. Yao, Q. Liu, J. Gu, R. Luo, J. Li, X. Yan, W. Wang, P. Liu, B. Chen, W. Zhang, W. Abbas, R. Naz and D. Zhang, *Angew Chem Int Ed Engl*, 2018, **57**, 6115-6119.
68. Z. Yang, A. Liu, C. Wang, F. Liu, J. He, S. Li, J. Wang, R. You, X. Yan, P. Sun, Y. Duan and G. Lu, *ACS Sens*, 2019, **4**, 1261-1269.
69. S. Li, P. Tuo, J. Xie, X. Zhang, J. Xu, J. Bao, B. Pan and Y. Xie, *Nano Energy*, 2018, **47**, 512-518.
70. J. Ran, G. Gao, F.-T. Li, T.-Y. Ma, A. Du and S.-Z. Qiao, *Nature Communications*, 2017, **8**, 13907.
71. X. Xie and N. Zhang, *Advanced Functional Materials*, 2020, **30**, 2002528.
72. Y. Xiang, L. Fang, F. Wu, S. Zhang, H. Ruan, H. Luo, H. Zhang, W. Li, X. Long, B. Hu and M. Zhou, *Adv Mater Technol-Us*, 2021, **6**.
73. C. Xue, Y. He, Y. Liu, P. Saha and Q. Cheng, *Ionics*, 2019, **25**, 3069-3077.
74. M. Ming, Y. Ren, M. Hu, Y. Zhang, T. Sun, Y. Ma, X. Li, W. Jiang, D. Gao, J. Bi and G. Fan, *Applied Catalysis B: Environmental*, 2017, **210**, 462-469.
75. H. Wang, Y. Wu, J. Zhang, G. Li, H. Huang, X. Zhang and Q. Jiang, *Mater Lett*, 2015, **160**, 537-540.
76. Z. Jin, C. Liu, Z. Liu, J. Han, Y. Fang, Y. Han, Y. Niu, Y. Wu, C. Sun and Y. Xu, *Adv Energy Mater*, 2020, **10**.

77. G. Zhang, T. Wang, Z. Xu, M. Liu, C. Shen and Q. Meng, *Chem Commun (Camb)*, 2020, **56**, 11283-11286.
78. P. Lian, Y. Dong, Z.-S. Wu, S. Zheng, X. Wang, W. Sen, C. Sun, J. Qin, X. Shi and X. Bao, *Nano Energy*, 2017, **40**, 1-8.
79. M. Lu, Y. Zhang, J. Chen, W. Han, W. Zhang, H. Li, X. Zhang and B. Zhang, *J Energy Chem*, 2020, **49**, 358-364.
80. Q. Tang, Z. Sun, S. Deng, H. Wang and Z. Wu, *J Colloid Interface Sci*, 2020, **564**, 406-417.
81. M. Ye, X. Wang, E. Liu, J. Ye and D. Wang, *ChemSusChem*, 2018, **11**, 1606-1611.
82. Q. Zhong, Y. Li and G. Zhang, *Chemical Engineering Journal*, 2021, **409**, 128099.
83. C. Peng, T. Zhou, P. Wei, H. Ai, B. Zhou, H. Pan, W. Xu, J. Jia, K. Zhang, H. Wang and H. Yu, *Chemical Engineering Journal*, 2022, **439**, 135685.
84. T. Hu, Z. Li, M. Hu, J. Wang, Q. Hu, Q. Li and X. Wang, *The Journal of Physical Chemistry C*, 2017, **121**, 19254-19261.
85. M. Ashton, K. Mathew, R. G. Hennig and S. B. Sinnoet, *J Phys Chem C*, 2016, **120**, 3550-3556.
86. I. Persson, L.-Å. Näslund, J. Halim, M. W. Barsoum, V. Darakchieva, J. Palisaitis, J. Rosen and P. O. Å. Persson, *2D Materials*, 2017, **5**.
87. J. Zhou, X. Zha, F. Y. Chen, Q. Ye, P. Eklund, S. Du and Q. Huang, *Angew Chem Int Ed Engl*, 2016, **55**, 5008-5013.
88. M. Seredych, C. E. Shuck, D. Pinto, M. Alhabeb, E. Precetti, G. Deysher, B. Anasori, N. Kurra and Y. Gogotsi, *Chemistry of Materials*, 2019, **31**, 3324-3332.
89. Y. Sun, D. Jin, Y. Sun, X. Meng, Y. Gao, Y. Dall'Agnese, G. Chen and X.-F. Wang, *Journal of Materials Chemistry A*, 2018, **6**, 9124-9131.
90. S. Lai, J. Jeon, S. K. Jang, J. Xu, Y. J. Choi, J. H. Park, E. Hwang and S. Lee, *Nanoscale*, 2015, **7**, 19390-19396.
91. W. Sun, S. A. Shah, Y. Chen, Z. Tan, H. Gao, T. Habib, M. Radovic and M. J. Green, *J. Mater. Chem. A*, 2017, **5**, 21663-21668.
92. Z. Sun, M. Yuan, L. Lin, H. Yang, C. Nan, H. Li, G. Sun and X. Yang, *ACS Materials Letters*, 2019, **1**, 628-632.
93. T. Yin, Y. Li, R. Wang, O. A. Al-Hartomy, A. Al-Ghamdi, S. Wageh, X. Luo, X. Tang and H. Zhang, *Ceramics International*, 2021, **47**, 28642-28649.
94. S. Y. Pang, Y. T. Wong, S. Yuan, Y. Liu, M. K. Tsang, Z. Yang, H. Huang, W. T. Wong and J. Hao, *J Am Chem Soc*, 2019, **141**, 9610-9616.
95. C. Wang, H. Shou, S. Chen, S. Wei, Y. Lin, P. Zhang, Z. Liu, K. Zhu, X. Guo, X. Wu, P. M. Ajayan and L. Song, *Adv Mater*, 2021, **33**, e2101015.
96. V. Kamysbayev, A. S. Filatov, H. Hu, X. Rui, F. Lagunas, D. Wang, R. F. Klie and D. V. Talapin, *Science*, 2020, **369**, 979-983.
97. M. Li, J. Lu, K. Luo, Y. Li, K. Chang, K. Chen, J. Zhou, J. Rosen, L. Hultman, P. Eklund, P. O. A. Persson, S. Du, Z. Chai, Z. Huang and Q. Huang, *J Am Chem Soc*, 2019, **141**, 4730-4737.
98. J. Lu, I. Persson, H. Lind, J. Palisaitis, M. Li, Y. Li, K. Chen, J. Zhou, S. Du, Z. Chai, Z. Huang, L. Hultman, P. Eklund, J. Rosen, Q. Huang and P. O. Å. Persson, *Nanoscale Advances*, 2019, **1**, 3680-3685.
99. Y. Li, H. Shao, Z. Lin, J. Lu, L. Liu, B. Duployer, P. O. A. Persson, P. Eklund, L. Hultman, M. Li, K. Chen, X. H. Zha, S. Du, P. Rozier, Z. Chai, E. Raymundo-Pinero, P. L. Taberna, P. Simon and Q. Huang, *Nat Mater*, 2020, **19**, 894-899.
100. H. Dong, P. Xiao, N. Jin, B. Wang, Y. Liu and Z. Lin, *Chemelectrochem*, 2021, **8**, 957-962.

101. H. Yu, Y. H. Wang, Y. Jing, J. M. Ma, C. F. Du and Q. Y. Yan, *Small*, 2019, **15**.
102. L. Verger, C. Xu, V. Natu, H. M. Cheng, W. C. Ren and M. W. Barsoum, *Curr Opin Solid St M*, 2019, **23**, 149-163.
103. P. O. A. Persson and J. Rosen, *Curr Opin Solid St M*, 2019, **23**.
104. M. Benchakar, L. Loupias, C. Garnero, T. Bilyk, C. Morais, C. Canaff, N. Guignard, S. Morisset, H. Pazniak, S. Hurand, P. Chartier, J. Pacaud, V. Mauchamp, M. W. Barsoum, A. Habrioux and S. Celerier, *Applied Surface Science*, 2020, **530**.
105. H. Wang, J. Zhang, Y. Wu, H. Huang, G. Li, X. Zhang and Z. Wang, *Applied Surface Science*, 2016, **384**, 287-293.
106. Y. Lei, Y. Cui, Q. Huang, J. Dou, D. Gan, F. Deng, M. Liu, X. Li, X. Zhang and Y. Wei, *Ceramics International*, 2019, **45**, 17653-17661.
107. K. Chen, X. Yan, J. Li, T. Jiao, C. Cai, G. Zou, R. Wang, M. Wang, L. Zhang and Q. Peng, *Nanomaterials (Basel)*, 2019, **9**.
108. H. Wang, J. Zhang, Y. Wu, H. Huang and Q. Jiang, *Journal of Physics and Chemistry of Solids*, 2018, **115**, 172-179.
109. S. Kumar, Y. Lei, N. H. Alshareef, M. A. Quevedo-Lopez and K. N. Salama, *Biosens Bioelectron*, 2018, **121**, 243-249.
110. Q. Wu, N. Li, Y. Wang, Y. Xu, J. Wu, G. Jia, F. Ji, X. Fang, F. Chen and X. Cui, *Anal Chem*, 2020, **92**, 3354-3360.
111. L. Zong, H. Wu, H. Lin and Y. Chen, *Nano Research*, 2018, **11**, 4149-4168.
112. K. Li, G. Zou, T. Jiao, R. Xing, L. Zhang, J. Zhou, Q. Zhang and Q. Peng, *Colloids and Surfaces A: Physicochemical and Engineering Aspects*, 2018, **553**, 105-113.
113. D. Gan, Q. Huang, J. Dou, H. Huang, J. Chen, M. Liu, Y. Wen, Z. Yang, X. Zhang and Y. Wei, *Applied Surface Science*, 2020, **504**.
114. P. Zhang, L. Wang, K. Du, S. Wang, Z. Huang, L. Yuan, Z. Li, H. Wang, L. Zheng, Z. Chai and W. Shi, *J Hazard Mater*, 2020, **396**, 122731.
115. B. Scheibe, K. Tadyszak, M. Jarek, N. Michalak, M. Kempiński, M. Lewandowski, B. Peplińska and K. Chybczyńska, *Applied Surface Science*, 2019, **479**, 216-224.
116. J. N. Xuan, Z. Q. Wang, Y. Y. Chen, D. J. Liang, L. Cheng, X. J. Yang, Z. Liu, R. Z. Ma, T. Sasaki and F. X. Geng, *Angew Chem Int Edit*, 2016, **55**, 14569-14574.
117. G. Liu, J. Zou, Q. Tang, X. Yang, Y. Zhang, Q. Zhang, W. Huang, P. Chen, J. Shao and X. Dong, *ACS Appl Mater Interfaces*, 2017, **9**, 40077-40086.
118. X. Yu, X. Cai, H. Cui, S. W. Lee, X. F. Yu and B. Liu, *Nanoscale*, 2017, **9**, 17859-17864.
119. F. Han, S. Luo, L. Xie, J. Zhu, W. Wei, X. Chen, F. Liu, W. Chen, J. Zhao, L. Dong, K. Yu, X. Zeng, F. Rao, L. Wang and Y. Huang, *ACS Appl Mater Interfaces*, 2019, **11**, 8443-8452.
120. H. Lin, X. Wang, L. Yu, Y. Chen and J. Shi, *Nano Lett*, 2017, **17**, 384-391.
121. H. Lin, Y. Wang, S. Gao, Y. Chen and J. Shi, *Adv Mater*, 2018, **30**.
122. C. Dai, H. Lin, G. Xu, Z. Liu, R. Wu and Y. Chen, *Chemistry of Materials*, 2017, **29**, 8637-8652.
123. C. Dai, Y. Chen, X. Jing, L. Xiang, D. Yang, H. Lin, Z. Liu, X. Han and R. Wu, *ACS Nano*, 2017, **11**, 12696-12712.
124. Z. Liu, H. Lin, M. Zhao, C. Dai, S. Zhang, W. Peng and Y. Chen, *Theranostics*, 2018, **8**, 1648-1664.
125. L. Bai, W. Yi, T. Sun, Y. Tian, P. Zhang, J. Si, X. Hou and J. Hou, *J Mater Chem B*, 2020, **8**, 6402-6417.
126. Y. Liu, Z. Dai, W. Zhang, Y. Jiang, J. Peng, D. Wu, B. Chen, W. Wei, X. Chen, Z. Liu, Z. Wang, F. Han, D. Ding, L. Wang, L. Li, Y. Yang and Y. Huang, *ACS Nano*, 2021, DOI: 10.1021/acsnano.1c02215.

127. J. Zhao, Y. Yang, C. Yang, Y. Tian, Y. Han, J. Liu, X. Yin and W. Que, *Journal of Materials Chemistry A*, 2018, **6**, 16196-16204.
128. Z. Nasri, E. Shams and M. Ahmadi, *J Electroanal Chem*, 2013, **703**, 146-152.
129. Z. Nasri and E. Shams, *Electrochim Acta*, 2013, **112**, 640-647.
130. Y. A. Atmane, L. Sicard, A. Lamouri, J. Pinson, M. Sicard, C. Masson, S. Nowak, P. Decorse, J. Y. Piquemal, A. Galtayries and C. Mangeney, *J Phys Chem C*, 2013, **117**, 26000-26006.
131. F. Shirini, M. Abedini and S. A. Kiaroudi, *Phosphorus Sulfur*, 2014, **189**, 1279-1288.
132. E. Tabrizian and A. Amoozadeh, *Rsc Adv*, 2016, **6**, 96606-96615.
133. M. Naguib, R. R. Unocic, B. L. Armstrong and J. Nanda, *Dalton Trans*, 2015, **44**, 9353-9358.
134. M. Mas-Montoya and R. A. J. Janssen, *Adv Funct Mater*, 2017, **27**.
135. F. P. OuYang, B. Huang, Z. Y. Li, J. Xiao, H. Y. Wang and H. Xu, *J Phys Chem C*, 2008, **112**, 12003-12007.
136. H. K. Choi, Y. Oh, H. Jung, H. Hong, B. C. Ku, N. H. You, Y. K. Kim, E. S. Shin and J. Yu, *Phys Chem Chem Phys*, 2018, **20**, 28616-28622.
137. Y. Wang, S. S. Li, H. Y. Yang and J. Luo, *Rsc Adv*, 2020, **10**, 15328-15345.
138. S. J. Jeon, S. Y. Kwak, D. Yim, J. M. Ju and J. H. Kim, *J Am Chem Soc*, 2014, **136**, 10842-10845.
139. L. Wang, W. Q. Tao, L. Y. Yuan, Z. R. Liu, Q. Huang, Z. F. Chai, J. K. Gibson and W. Q. Shi, *Chem Commun*, 2017, **53**, 12084-12087.
140. S. H. I. Wei-Qun, W. Hong-Qing, W. Lin and S. Huan, *Journal of Inorganic Materials*, 2019, DOI: 10.15541/jim20190073.
141. Y. Dall'Agnese, P. Rozier, P. L. Taberna, Y. Gogotsi and P. Simon, *J Power Sources*, 2016, **306**, 510-515.
142. L. Y. Yu, L. F. Hu, B. Anasori, Y. T. Liu, Q. Z. Zhu, P. Zhang, Y. Gogotsi and B. Xu, *Acs Energy Lett*, 2018, **3**, 1597-1603.
143. Z. Y. Wang, S. Qin, S. Seyedin, J. Z. Zhang, J. T. Wang, A. Levitt, N. Li, C. Haines, R. Ovalle-Robles, W. W. Lei, Y. Gogotsi, R. H. Baughman and J. M. Razal, *Small*, 2018, **14**.
144. A. M. Navarro-Suarez, K. Maleski, T. Makaryan, J. Yan, B. Anasori and Y. Gogotsi, *Batteries Supercaps*, 2018, **1**, 33-38.
145. Z. F. Lin, D. Barbara, P. L. Taberna, K. L. Van Aken, B. Anasori, Y. Gogotsi and P. Simon, *J Power Sources*, 2016, **326**, 575-579.
146. Q. Jiang, N. Kurra, M. Alhabeb, Y. Gogotsi and H. N. Alshareef, *Adv Energy Mater*, 2018, **8**.
147. J. Li, X. L. Wang, T. Zhang, C. L. Wang, Z. J. Huang, X. Luo and Y. H. Deng, *Asian J Pharm Sci*, 2015, **10**, 81-98.
148. S. Khemakhem and R. Ben Amar, *Ceramics International*, 2011, **37**, 3323-3328.
149. K. Rajavel, X. Yu, P. Zhu, Y. Hu, R. Sun and C. Wong, *ACS Applied Materials & Interfaces*, 2020, **12**, 49737-49747.
150. R. Khaledialidusti, A. K. Mishra and A. Barnoush, *Journal of Materials Chemistry C*, 2020, **8**, 4771-4779.
151. X. Zou and B. I. Yakobson, *Accounts of Chemical Research*, 2015, **48**, 73-80.
152. M. Tripathi, F. Lee, A. Michail, D. Anestopoulos, J. G. McHugh, S. P. Ogilvie, M. J. Large, A. A. Graf, P. J. Lynch, J. Parthenios, K. Papagelis, S. Roy, M. A. S. R. Saadi, M. M. Rahman, N. M. Pugno, A. A. K. King, P. M. Ajayan and A. B. Dalton, *ACS Nano*, 2021, **15**, 2520-2531.
153. H. I. Rasool, C. Ophus and A. Zettl, *Advanced Materials*, 2015, **27**, 5771-5777.
154. E. Mitterreiter, B. Schuler, K. A. Cochrane, U. Wurstbauer, A. Weber-Bargioni, C. Kastl and A. W.

Holleitner, *Nano Letters*, 2020, **20**, 4437-4444.
155. M. R. Rosenberger, H.-J. Chuang, K. M. McCreary, C. H. Li and B. T. Jonker, *ACS Nano*, 2018, **12**, 1793-1800.
156. R. Chua, J. Yang, X. He, X. Yu, W. Yu, F. Bussolotti, P. K. J. Wong, K. P. Loh, M. B. H. Breese, K. E. J. Goh, Y. L. Huang and A. T. S. Wee, *Advanced Materials*, 2020, **32**, 2000693.
157. Y. Dong, S. Zhang, X. Du, S. Hong, S. Zhao, Y. Chen, X. Chen and H. Song, *Advanced Functional Materials*, 2019, **29**, 1901127.
158. L. Nguyen, H.-P. Komsa, E. Khestanova, R. J. Kashtiban, J. J. P. Peters, S. Lawlor, A. M. Sanchez, J. Sloan, R. V. Gorbachev, I. V. Grigorieva, A. V. Krasheninnikov and S. J. Haigh, *ACS Nano*, 2017, **11**, 2894-2904.
159. N. H. Kwon, S.-J. Shin, X. Jin, Y. Jung, G.-S. Hwang, H. Kim and S.-J. Hwang, *Applied Catalysis B: Environmental*, 2020, **277**, 119191.
160. L. H. Karlsson, J. Birch, J. Halim, M. W. Barsoum and P. O. Å. Persson, *Nano Letters*, 2015, **15**, 4955-4960.
161. X. Sang, Y. Xie, M.-W. Lin, M. Alhabeb, K. L. Van Aken, Y. Gogotsi, P. R. C. Kent, K. Xiao and R. R. Unocic, *ACS Nano*, 2016, **10**, 9193-9200.
162. D. Zhao, Z. Chen, W. Yang, S. Liu, X. Zhang, Y. Yu, W.-C. Cheong, L. Zheng, F. Ren, G. Ying, X. Cao, D. Wang, Q. Peng, G. Wang and C. Chen, *Journal of the American Chemical Society*, 2019, **141**, 4086-4093.
163. A. Bandyopadhyay, D. Ghosh and S. K. Pati, *Physical Chemistry Chemical Physics*, 2018, **20**, 4012-4019.
164. X. Fu, H. Chang, Z. Shang, P. Liu, J. Liu and H. a. Luo, *Chemical Engineering Journal*, 2020, **381**, 122001.
165. X. Tang, D. Zhou, P. Li, X. Guo, B. Sun, H. Liu, K. Yan, Y. Gogotsi and G. Wang, *Advanced Materials*, 2020, **32**, 1906739.
166. J. Tang, T. Mathis, X. Zhong, X. Xiao, H. Wang, M. Anayee, F. Pan, B. Xu and Y. Gogotsi, *Advanced Energy Materials*, 2021, **11**, 2003025.
167. W. Cui, Z.-Y. Hu, R. R. Unocic, G. Van Tendeloo and X. Sang, *Chinese Chemical Letters*, 2021, **32**, 339-344.
168. C. Qiao, H. Wu, X. Xu, Z. Guan and W. Ou-Yang, *Advanced Materials Interfaces*, 2021, **8**, 2100903.
169. A. Lipatov, M. Alhabeb, M. R. Lukatskaya, A. Boson, Y. Gogotsi and A. Sinitskii, *Advanced Electronic Materials*, 2016, **2**, 1600255.
170. N. Chen, Y. Zhou, S. Zhang, H. Huang, C. Zhang, X. Zheng, X. Chu, H. Zhang, W. Yang and J. Chen, *Nano Energy*, 2021, **85**, 106007.
171. Y. Tang, C. Yang, X. Xu, Y. Kang, J. Henzie, W. Que and Y. Yamauchi, *Advanced Energy Materials*, 2022, **12**, 2103867.
172. Y. Fang, Y. Cao, B. Tan and Q. Chen, *ACS Applied Materials & Interfaces*, 2021, **13**, 42624-42634.
173. Z. Yang, H. Zou, Y. Zhang, F. Liu, J. Wang, S. Lv, L. Jiang, C. Wang, X. Yan, P. Sun, L. Zhang, Y. Duan and G. Lu, *Advanced Functional Materials*, 2021, 2108959.
174. Q. Tao, M. Dahlqvist, J. Lu, S. Kota, R. Meshkian, J. Halim, J. Palisaitis, L. Hultman, M. W. Barsoum, P. O. Å. Persson and J. Rosen, *Nature Communications*, 2017, **8**, 14949.
175. Z. Zhang, H. Li, G. Zou, C. Fernandez, B. Liu, Q. Zhang, J. Hu and Q. Peng, *ACS Sustainable Chemistry & Engineering*, 2016, **4**, 6763-6771.
176. J. Zhang, Y. Zhao, X. Guo, C. Chen, C.-L. Dong, R.-S. Liu, C.-P. Han, Y. Li, Y. Gogotsi and G. Wang,

Nature Catalysis, 2018, **1**, 985-992.
177. A. Wang, J. Li and T. Zhang, *Nature Reviews Chemistry*, 2018, **2**, 65-81.
178. Y. Liu, Y.-H. Li, X. Li, Q. Zhang, H. Yu, X. Peng and F. Peng, *ACS Nano*, 2020, **14**, 14181-14189.
179. W. Peng, M. Luo, X. Xu, K. Jiang, M. Peng, D. Chen, T.-S. Chan and Y. Tan, *Advanced Energy Materials*, 2020, **10**, 2001364.
180. Y. Shi and Y. Liu, *Applied Catalysis B: Environmental*, 2021, **297**, 120482.
181. F. Xia, J. Lao, R. Yu, X. Sang, J. Luo, Y. Li and J. Wu, *Nanoscale*, 2019, **11**, 23330-23337.
182. Y. Chae, S. J. Kim, S.-Y. Cho, J. Choi, K. Maleski, B.-J. Lee, H.-T. Jung, Y. Gogotsi, Y. Lee and C. W. Ahn, *Nanoscale*, 2019, **11**, 8387-8393.
183. C. J. Zhang, S. Pinilla, N. McEvoy, C. P. Cullen, B. Anasori, E. Long, S.-H. Park, A. Seral-Ascaso, A. Shmeliov, D. Krishnan, C. Morant, X. Liu, G. S. Duesberg, Y. Gogotsi and V. Nicolosi, *Chemistry of Materials*, 2017, **29**, 4848-4856.
184. S. Huang and V. N. Mochalin, *Inorganic Chemistry*, 2019, **58**, 1958-1966.
185. I. Persson, J. Halim, T. W. Hansen, J. B. Wagner, V. Darakchieva, J. Palisaitis, J. Rosen and P. O. Å. Persson, *Advanced Functional Materials*, 2020, **30**, 1909005.
186. H. Ghassemi, W. Harlow, O. Mashtalir, M. Beidaghi, M. R. Lukatskaya, Y. Gogotsi and M. L. Taheri, *Journal of Materials Chemistry A*, 2014, **2**, 14339-14343.
187. B. Ahmed, D. H. Anjum, Y. Gogotsi and H. N. Alshareef, *Nano Energy*, 2017, **34**, 249-256.
188. J. Guo, B. Legum, B. Anasori, K. Wang, P. Lelyukh, Y. Gogotsi and C. A. Randall, *Advanced Materials*, 2018, **30**, 1801846.
189. K. Rajavel, Y. Hu, P. Zhu, R. Sun and C. Wong, *Chemical Engineering Journal*, 2020, **399**, 125791.
190. X. Guo, J. Zhang, J. Song, W. Wu, H. Liu and G. Wang, *Energy Storage Materials*, 2018, **14**, 306-313.
191. C. Zhang, M. Beidaghi, M. Naguib, M. R. Lukatskaya, M.-Q. Zhao, B. Dyatkin, K. M. Cook, S. J. Kim, B. Eng, X. Xiao, D. Long, W. Qiao, B. Dunn and Y. Gogotsi, *Chemistry of Materials*, 2016, **28**, 3937-3943.
192. T. Su, R. Peng, Z. D. Hood, M. Naguib, I. N. Ivanov, J. K. Keum, Z. Qin, Z. Guo and Z. Wu, *ChemSusChem*, 2018, **11**, 688-699.
193. Y. Fang, Z. Liu, J. Han, Z. Jin, Y. Han, F. Wang, Y. Niu, Y. Wu and Y. Xu, *Advanced Energy Materials*, 2019, **9**, 1803406.
194. A. Sokolov, M. Ali, H. Li, Y.-R. Jeon, M. J. Ko and C. Choi, *Advanced Electronic Materials*, 2021, **7**, 2000866.
195. W. Zhang, J. Peng, W. Hua, Y. Liu, J. Wang, Y. Liang, W. Lai, Y. Jiang, Y. Huang, W. Zhang, H. Yang, Y. Yang, L. Li, Z. Liu, L. Wang and S.-L. Chou, *Advanced Energy Materials*, 2021, **11**, 2100757.
196. L. Yang, D. Kan, C. Dall'Agnese, Y. Dall'Agnese, B. Wang, A. K. Jena, Y. Wei, G. Chen, X.-F. Wang, Y. Gogotsi and T. Miyasaka, *Journal of Materials Chemistry A*, 2021, **9**, 5016-5025.
197. Q. Wang, Y. Xiong, J. Xu, F. Dong and Y. Xiong, *Separation and Purification Technology*, 2022, **286**, 120506.
198. A. Olshtrem, S. Chertopalov, O. Guselnikova, R. R. Valiev, M. Cieslar, E. Miliutina, R. Elashnikov, P. Fitl, P. Postnikov, J. Lancok, V. Svorcik and O. Lyutakov, *2D Materials*, 2021, **8**, 045037.
199. H. Chen, Y. Wen, Y. Qi, Q. Zhao, L. Qu and C. Li, *Advanced Functional Materials*, 2020, **30**, 1906996.
200. J. Kim, Y. Yoon, S. K. Kim, S. Park, W. Song, S. Myung, H.-K. Jung, S. S. Lee, D. H. Yoon and K.-S. An, *Advanced Functional Materials*, 2021, **31**, 2008722.
201. M. C. Krecker, D. Bukharina, C. B. Hatter, Y. Gogotsi and V. V. Tsukruk, *Advanced Functional Materials*, 2020, **30**, 2004554.

202. X. Yang, Q. Wang, K. Zhu, K. Ye, G. Wang, D. Cao and J. Yan, *Advanced Functional Materials*, 2021, **31**, 2101087.
203. T. Hu, J. Yang and X. Wang, *Physical Chemistry Chemical Physics*, 2017, **19**, 31773-31780.
204. R. Hu, Y. H. Li, Z. H. Zhang, Z. Q. Fan and L. Sun, *Journal of Materials Chemistry C*, 2019, **7**, 7745-7759.
205. V. Parey, B. M. Abraham, S. H. Mir and J. K. Singh, *ACS Applied Materials & Interfaces*, 2021, **13**, 35585-35594.
206. H. Chen, A. D. Handoko, T. Wang, J. Qu, J. Xiao, X. Liu, D. Legut, Z. Wei Seh and Q. Zhang, *ChemSusChem*, 2020, **13**, 5690-5698.
207. X. Qian, L. Li, Y. Li, Z. Liu, Z. Tian, C. Zhan and L. Chen, *Physical Chemistry Chemical Physics*, 2021, **23**, 12431-12438.
208. L. Li, B. Li, H. Guo, Y. Li, C. Sun, Z. Tian and L. Chen, *Nanoscale*, 2020, **12**, 15880-15887.
209. S. Tang, T. Liu, Q. Dang, X. Zhou, X. Li, T. Yang, Y. Luo, E. Sharman and J. Jiang, *The Journal of Physical Chemistry Letters*, 2020, **11**, 5051-5058.
210. C. Cheng, X. Zhang, Z. Yang and Z. Zhou, *ACS Applied Materials & Interfaces*, 2018, **10**, 32903-32912.